The final publication is available at

https://doi.org/10.1016/j.combustflame.2021.111561

Additional Information

Title: *Fundamental Insights on Ignition and Combustion of Natural Gas in an Active Fueled Pre-chamber Spark-Ignition System*

Authors and Affiliations:

- **Rajavasanth Rajasegar:** Combustion Research Facility, Sandia National Laboratories, Livermore, CA, 94550, USA.

- **Yoichi Niki:** National Institute of Maritime, Port and Aviation Technology, Tokyo, 181-0004, Japan.

- **Jose Maria Garcia Oliver:** CMT - Motores Térmicos, Universitat Politècnica de València, Valencia, 46022, Spain.

- **Zheming Li:** Combustion Research Facility, Sandia National Laboratories, Livermore, CA, 94550, USA.

- **Mark P. B. Musculus:** Combustion Research Facility, Sandia National Laboratories, Livermore, CA, 94550, USA.

Corresponding Author

- **Rajavasanth Rajasegar**

  Combustion Research Facility

  Sandia National Laboratories

  Livermore, CA, 94550, USA

  Phone: +1-925-294-6401

  E-mail: rrajase@sandia.gov

Fundamental Insights on Ignition and Combustion of Natural Gas in an

Active Fueled Pre-chamber Spark-Ignition System

Rajavasanth Rajasegar[1], Yoichi Niki[2], Jose Maria Garcia Oliver [3], Zheming Li [1],

Mark P. B. Musculus [1]

[1]*Combustion Research Facility, Sandia National Laboratories, Livermore, CA, 94550, USA*

[2]*National Institute of Maritime, Port and Aviation Technology, Tokyo, 181-0004, Japan*

[3]*Universitat Politècnica de València, Valencia, 46022, Spain*

Abstract

Pre-chamber spark-ignition (PCSI), either fueled or non-fueled, is a leading concept with the potential to enable diesel-like efficiency in medium-duty (MD) and heavy-duty (HD) natural gas (NG) engines. However, the inadequate scientific base and simulation tools to describe/predict the underlying processes governing PCSI systems is one of the key barriers to market penetration of PCSI for MD/HD NG engines. To this end, experiments were performed in a heavy-duty, optical, single-cylinder engine fitted with an active fueled PCSI module. The spatial and temporal progress of ignition and subsequent combustion of lean-burn natural gas using PCSI system were studied using optical diagnostic imaging and heat release analysis based on main-chamber and pre-chamber pressure measurements.

Optical diagnostics involving simultaneous infrared (IR) and high-speed (30 kfps) broadband and filtered OH* chemiluminescence imaging are used to probe the combustion process. Following the early pressure rise in the pre-chamber, IR imaging reveals initial ejection of unburnt fuel-air mixture from the pre-chamber into the main-chamber. Following this, the pre-chamber gas jets exhibit chemical activity in the vicinity of the pre-chamber region followed by a delayed spread in OH* chemiluminescence, as they continue to penetrate further into the

main-chamber. The OH* signal progress radially until the pre-chamber jets merge, which sets up the limit to a first stage, jet-momentum driven, mixing-controlled (temperature field) premixed combustion. This is then followed by the subsequent deceleration of the pre-chamber jets, caused by the decrease in the driving pressure difference (ΔP) as well as charge entrainment, resulting in a flame front evolution, where mixing is not the only driver. Chemical-kinetic calculations probe the possibility of flame propagation or sequential auto-ignition in the second stage of combustion. Finally, key phenomenological features are then summarized so as to provide fundamental insights on the complex underlying fluid-mechanical and chemical-kinetic processes that govern the ignition and subsequent combustion of natural gas near lean-limits in high-efficiency lean-burn natural gas engines employing PCSI system.

Keywords:

Pre-chamber spark-ignition, lean-premixed natural gas combustion, broadband chemiluminescence, OH* chemiluminescence, infrared imaging, nixing-controlled, chemical kinetics

1. Introduction

Natural gas is becoming an increasingly important alternative fuel option to petroleum-based fuels for internal combustion engines due to a variety of reasons. Natural gas is one of the most abundant fossil fuels that requires relatively little processing prior to use [1]. At present, natural gas meets upwards of 35% of the energy demand in the United States [2]. Ever-increasing energy demands for both transportation and stationary applications, coupled with diminishing reserves of petroleum-based fuels, make natural gas an attractive alternate fuel [2]. Further, due to the high hydrogen to carbon ratio, natural gas produces 25 to 30% less CO_2 emissions per unit energy than gasoline and diesel fuels, while emissions of sulfur oxides, soot, and other particulate

matter are virtually non-existent, and may thus have an overall positive impact on the environment [3-6].

However, when operated under rich or near-stoichiometric conditions of fuel and air mixture, natural gas engines suffer from lower fuel efficiency and limited operating load range due to lower compression ratio, throttling losses, engine knock, high nitrogen oxides (NO_x) emissions, and excessive exhaust gas temperatures caused by lower thermal efficiency [7-9]. Thus, in recent years, to comply with increasingly stringent scrutiny and regulation of medium and heavy-duty vehicle exhaust emissions and fuel-economy standards, there has been an increased interest among engine manufacturers in adopting the lean-burn strategy in which fuel is burnt in excess air. This yields lower combustion temperatures that minimizes NO_x emissions [10, 11], and results in higher thermal efficiency due to lower heat losses through the combustion chamber walls, increase in specific heat ratio, and reduced pumping losses at part-loads due to throttle-less operation [12-14]. Furthermore, lean-burn strategy also allows for knock mitigation thus enabling high load operation and/or higher compression ratios [12-14].

However, lean-burn technology also poses some serious challenges in terms of combustion stability and requires more involved exhaust after-treatments systems to comply with stringent emission regulations [15]. Thus, to fulfill NO_x emissions regulation, it is necessary to operate at excess dilution ($\lambda \sim 1.8 - 2.0$) that may exceed the lean operational (stability) limit ($\lambda \sim 1.4$) of conventional spark-ignition (SI) engines [15]. However, since the effectiveness of the three-way catalyst, which is the primary means to control NO_x, UHC, and CO emissions in conventional SI engines, degrades precipitously at air-fuel ratios that vary from stoichiometric, it is incompatible with the lean-burn concept [15]. Moreover, increased dilution leads to critical ignition and flame propagation issues as it becomes increasingly difficult to ignite leaner fuel-air mixtures reliably.

Unstable ignition or failure to ignite the lean mixture can often lead to poor combustion stability due to increased probability of flame quenching, partial burn cycles, or misfires, which can result in undesirable effects such as increased cycle-to-cycle variability, rough operation, reduction in thermal efficiency, and increased unburned hydrocarbon (UHC) emissions [16-18]. Partial burning is primarily due to slower laminar flame speeds of lean mixtures that severely hamper flame kernel growth and thus flame propagation. This is further intensified due to the lower laminar flame speeds of natural gas when compared to other hydrocarbon fuels (~ 15% lower than gasoline at stoichiometric conditions) due to its higher activation energy that is more pronounced under lean conditions [19]. Thus, the lean limit of natural gas is limited by the capability of the ignition system to reliably ignite the fuel-lean mixtures [7-9].

To overcome these difficulties, advanced ignition systems like diesel pilot-fuel injections [20-24] or pre-chamber spark-ignition [25, 26] can be utilized to promote ignition enhancement, faster burning rates, and stable combustion by distributing the ignition source over many ignition sites. Pre-chamber spark-ignition (PCSI) systems, also known as turbulent jet ignition systems [25, 26], offer a relatively more simplified solution as it requires minimum to no engine modification. It is structurally less complex than diesel pilot-fuel injection systems that are primarily well suited for natural gas engines used in stationary and marine applications due to fewer space constraints and ease of handling two fueling sub-systems [7, 8]. PCSI systems employ a pre-chamber, which is a dedicated small volume chamber that is connected to the main combustion chamber through one or more small orifices, and houses a spark plug and a fuel injector (for fueled PCSI systems). PCSI systems typically utilize a single fuel, and successful ignition is achieved by means of spark ignition of a premixed charge present in an actively [12, 13] or passively [27] fueled pre-chamber. In an active fueled PCSI system, the dedicated fuel injector helps in controlling the air-to-fuel ratio

inside the pre-chamber at near stoichiometry independent of the main-chamber charge composition, whereas in a passive fueled PCSI system, there is no additional fuel injector, which reduces the complexity, but charge composition inside the pre-chamber is not directly controlled.

The combustion initiated inside the pre-chamber creates a rapid rise in its pressure and temperature, thereby generating a driving force that forces the pre-chamber gases into the main-chamber through the orifices in the form of transient turbulent jets. These pre-chamber jets penetrate into the main-chamber charge, and serve as a distributed ignition source for the onset of combustion in multiple locations through a complex coupling of turbulence generation, chemical kinetics, and thermal effects [25, 26]. Due to the turbulent nature of the jet, the ignition kernels generated on the surface of the jet are comprised of a wide range of length and velocity scales [18], which ensure ignition of the main-chamber charge as the unburned mixture becomes entrained [28]. The ejected pre-chamber gas jets act as important drivers of the reaction front throughout the main-chamber, both in terms of momentum as well as turbulence enhancers. This causes the reaction front to sweep faster through the unburned mixture, allowing for shorter combustion durations even in traditionally slow burning lean mixtures [29], and hence results in in rapid pressure rise and heat release, and in some cases enhanced auto-ignition [30, 31] resulting in increased burn rates, enhanced combustion stability, with minimal cycle-to-cycle variability [25, 26]. Thus by providing a reliable, distributed ignition source for homogenous lean mixtures of natural gas, PCSI systems can offer increased burn rates, which in turn allows for increased levels of dilution (lean-burn and/or EGR) when compared to conventional SI combustion [12-14], which has facilitated the development of high-thermal efficiency, low NO_x emission, ultra-lean-burn natural gas engines.

Over the years, there have been several experimental and computational efforts focused on

various aspects of the PCSI systems that highlight its potential for ultra-lean combustion. These studies encompass fundamental work on turbulent jet development and ignition to performance, emissions characterization, and optimization efforts, carried out in a wide range of experimental facilities ranging from simple geometries such as a divided chamber [32-34], to rapid compression machines with optical access [28, 30, 31], optical engines [35, 36], and conventional full-scale metal engines [6, 14, 27, 37]. However, due to the complicated nature of the fundamental complex coupling between the physical and chemical processes that govern the ignition and subsequent combustion of natural gas near the lean limit, our understanding of PCSI systems is far from complete. Hence, a comprehensive and methodical effort is necessary to address our lack of understanding and the simulation tools that are required to describe / predict the fluid-mechanical and chemical-kinetic processes governing PCSI systems, which enable engineers in industry to optimize designs for efficiency, noise, reliability, pollutant formation, emissions control integration, and drivability [3-6]. This has been identified as one of the key barriers that has impeded market penetration of PCSI systems for medium and heavy-duty natural gas engines as outlined in the 2017 DOE Natural Gas Vehicle Research Workshop [38].

This work constitutes a small portion of a comprehensive integrated research plan that capitalizes on the existing expertise and core capabilities at four national laboratories (Sandia National Laboratories, Argonne National Laboratories, Oak Ridge National Laboratories and National Renewable Energy Laboratories) in metal- and optical-engine experiments, in-cylinder simulations using computational fluid dynamics (CFD) and chemical kinetics, bench-scale ignition experiments and simulations, and emissions-controls experiments. The overarching goal of this work is to provide fundamental insights on the ignition and subsequent combustion of natural gas near lean-limits in a heavy-duty, optical, single-cylinder engine fitted with an actively fueled PCSI

module. To this end, phenomenological features of the pre-chamber ignition and subsequent combustion process are presented based on optical diagnostic imaging and heat release analysis. In addition to in-cylinder pressure measurements, simultaneous infrared (IR) and high-speed chemiluminescence (both broadband and filtered OH*) imaging reveal how the pre-chamber ignition jets emerge from the pre-chamber, mixes with and ignites the premixed main-chamber charge, and subsequently drives the progression of main-chamber combustion, whether by flame propagation or sequential auto-ignition.

Unlike existing literature, which mostly relied on experiments performed in metal engines or in combustion vessels or in optical engines with limited optical diagnostics, this study aims to provide a detailed description of the underlying fluid-mechanical and chemical-kinetic processes that govern the ignition and subsequent combustion of natural gas near lean-limits using a PCSI system under realistic engine conditions. High-fidelity optical diagnostics are utilized to both quantitatively and qualitatively describe the different combustion phases, while resolving regions of burned gases from unburned fuel-air mixture. Finally, the main ideas are summarized into a phenomenological descriptions that help discern the sequence of events leading to ignition and subsequent combustion of a fuel-lean main-chamber mixture by a near-stoichiometric pre-chamber.

2. Experimental Overview

2.1. Optical Engine

The experiments use the Sandia-Cummins single-cylinder heavy-duty optical engine, which is modified from a single-cylinder Cummins N-series direct-injection, heavy-duty diesel engine. The optical engine has a 13.97-cm bore and 15.24-cm stroke, yielding a displacement of 2.34 L per cylinder with a base compression ratio of 11.22. The intake port geometry of the

production engine, which has a steady-state (i.e., measured on a flow-bench) swirl ratio of 0.5 [39], is preserved in the optical engine. The engine is equipped with a Bowditch piston with an open, right-cylindrical bowl and a flat fused-silica piston-crown window that allows unrestricted optical access to the whole bowl when viewed from below. Further, one of the two exhaust valves has been replaced with an optical window, which provides a view of the squish region from above (view not used in this study). Flat rectangular windows installed in a ring at the top of the cylinder provide additional laser access through the cylinder wall. Further details about this engine can be found elsewhere [40, 41]. A schematic layout of the optical engine fitted with PCSI system along with the imaging setups are shown in Figure 1 and the major specifications of the engine, pre-chamber system, and fuel injectors are tabulated in Table 1.

2.2. Pre-chamber Spark-Ignition and Fuel Injection Systems

The optical engine is fitted with a modular PCSI system equipped with a dedicated fuel injector, a sparkplug, and pressure transducer. The pre-chamber has an internal volume of 4.66 ml and protrudes 10.6 mm below the fire deck resulting in an effective compression ratio of 11.03. The pre-chamber has eight circular, 1.6-mm diameter nozzle orifices with included angle of 130º. A Bosch HDEV5 GDI, solenoid-actuated injector with 6 (3 pairs of spray plumes) unequally spaced 0.17-mm orifices is used for fast response time and its ability to deliver consistent, short-duration pre-chamber injections. A miniature Rimfire Z1 spark plug is chosen for its compact size, which allowed for easy installation inside the PCSI module. A Clean Air SP010, solenoid-actuated, single-hole gas injector fitted on the intake manifold 0.55 m upstream of the engine intake port fumigates the natural gas into the intake air stream using a perforated annular tube embedded in the intake flow. The location of the natural gas fumigation injector coupled with the long residence time from injection to induction into the engine (4-5 cycles) yields a fairly homogenous

premixed charge. The natural gas is a surrogate mixture of 95% methane, 4% ethane, and 1% propane by volume.
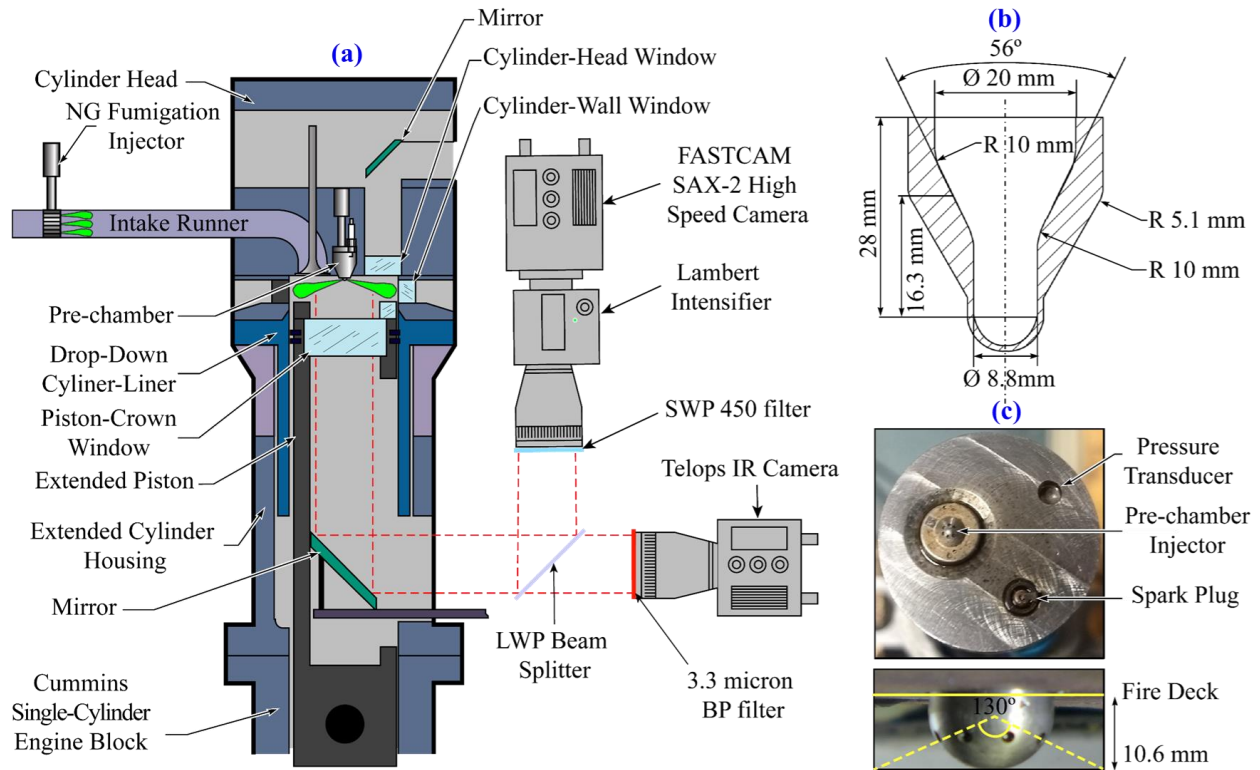

Figure 1. Schematic layout of the (a) optical engine and imaging setup, (b) internal geometry of the pre-chamber and (c) pre-chamber spark ignition system and its components as installed in the optical engine.

2.3. Diagnostics

Main-chamber and pre-chamber pressure measurements along with various optical imaging diagnostics measure the spatial and temporal ignition and subsequent combustion characteristics of lean-burn of natural gas using PCSI system. Main-chamber and pre-chamber pressure are measured with AVL QC34D piezoelectric pressure transducers and recorded every quarter crank angle degree (CAD). The apparent heat release rate (AHRR) is calculated from the combined pressure measurements using standard techniques identical to the indirect injection diesel engines approach [42]. Before computing the AHRR, the pressure data are smoothed using

a Fourier-series low-pass filter with a Gaussian roll-off function with 100% transmission from 0 to 800 Hz and dropping to 1% at 3360 Hz. Due to the relatively slow energy release at the operating conditions investigated here, the filtering scheme removes acoustic ringing with virtually no effect on the shape of the AHRR curve [43].

Engine Specifications	
Engine base type	Cummins N-14, DI diesel
Number of cylinders	1
Number of intake valves	2
Number of exhaust valves	1*
Combustion chamber	Quiescent, direct injection
Swirl ratio	0.5
Bowl width [cm]	9.78 cm
Bowl depth [cm]	1.55 cm
Bore $\times$ Stroke [cm]	13.97 $\times$15.24
Connecting rod length [cm]	30.48
Displacement [liters]	2.34
Base compression ratio	11.22
Pre-chamber Specifications	
Volume [ml]	4.66
Orifices and diameter [mm]	8 equally-spaced, 1.6
Included angle	130
Compression Ratio	11.03
Spark plug	Miniature rimfire Z1
Natural Gas Pre-chamber Injector Specifications	
Fuel injector type	Solenoid actuated, Bosch HDEV5 GDI Injector
Orifices and diameter [mm]	6 (3 identical pairs) unequally-spaced, 0.17
Fuel	Natural gas (95% CH_4, 4% C_2H_6 1% C_3H_8 by vol.)
Natural Gas Fumigation Injector Specifications	
Fuel injector type	Solenoid actuated, Clean Air SP010 Gas Injector
No of holes	1
Fuel	Natural gas (95% CH_4, 4% C_2H_6 1% C_3H_8 by vol.)
* In this optically accessible diesel engine, one of the two exhaust valves of the production cylinder head is replaced by a window.	

Table 1. Engine and injector specifications.

To quantify the in-cylinder premixed natural gas concentration and the spatial extent of the

pre-chamber jets (tip penetration, spreading angle), infrared (IR) C-H stretch emission images are captured by a Telops TS-IR MW InSb camera fitted with a Spectrogon band-pass filter (BPF) centered at 3.317 microns with 215 nm full width at half-maximum (FWHM). The BPF transmits infrared emission from natural gas arising from C-H vibrational stretching at elevated in-cylinder temperatures achieved the during compression process prior to combustion, as well as during the combustion process (other species may also contribute to the IR signal during combustion). The frame rate and resolution of the infrared camera are set to 10 fps and 640×512 pixels with one IR image captured every fired cycle.

Chemiluminescence imaging provides insight into the spatial and temporal ignition and subsequent combustion characteristics of the premixed charge in the main-chamber due to the transient pre-chamber jets. Crank-angle resolved broadband chemiluminescence [44] and filtered OH* chemiluminescence [45] images are captured in separate acquisitions by a Photron FASTCAM SA-X2 high-speed camera coupled to a Lambert Hi-CATT high-speed intensifier with a S-20 photocathode. The frame rate and resolution of the high-speed camera are set to 30000 fps and 768×512 pixels with chemiluminescence images captured every quarter crank angle degree. For the fueled pre-chamber experiments, OH* chemiluminescence is imaged using a 105 mm UV Nikkor lens with an aperture setting of f/4.5 in combination with a 310-nm BPF with a 10-nm FWHM. In the pre-chamber only fueling experiments, OH* chemiluminescence intensities are lower due to the minimal fueling involved. To overcome the reduced intensities, chemiluminescence imaging is carried out without any filters and a fully open aperture setting (f/2.5) using a 105 mm glass Nikkor lens, thereby collecting broadband chemiluminescence from HCHO*, HCO*, CH*, CO_2*, and/or broadband emission from the CO continuum [46, 47] in addition to OH* emission.

Despite the slow framing rate of the infrared camera, the combination of simultaneous infrared and chemiluminescence imaging allows tracking of the spatial and temporal evolution of pre-chamber ignition-jets in terms of the temperature field (qualitative) and active combustion species, respectively.

2.4. Engine Operating Conditions and Test Matrix

Experimental conditions	
Intake temperature [ºC]	41
Intake pressure [kPa]	105
Intake O_2 [%] (N_2 dil.)	21
Pre-chamber spark timing [CAD]	343
Main-chamber pressure at spark [bar]	19
Main-chamber temperature at spark [K]	730
Natural gas fumigation injector pressure [bar]	7.5
Natural gas fumigation injection SSE [CAD]	40
Natural gas pre-chamber injector pressure [bar]	100
Natural gas pre-chamber injection ESE [CAD]	336
Engine speed [RPM]	1200
Pre-chamber only fueling experiments	
Natural gas pre-chamber injection SSE [CAD]	325.75
Natural gas pre-chamber injection DSE [µs]	1517
Natural gas pre-chamber injection ESE [CAD]	336.50
Pre-chamber air-fuel ratio (λ_{PC})	0.93*
Pre-chamber fuel-air equivalence ratio (ϕ_{PC})	1.08*
Natural gas fumigation injection DSE [µs]	0
Main-chamber air-fuel ratio (λ_{MC})	∞ (No natural gas)
Main-chamber fuel-air equivalence ratio (ϕ_{MC})	0 (No natural gas)
Fueled pre-chamber experiments	
Natural gas pre-chamber injection SSE [CAD]	332.25 - 330
Natural gas pre-chamber injection DSE [µs]	612 - 917
Natural gas pre-chamber injection ESE [CAD]	336.5
Pre-chamber air-fuel ratio (λ_{PC})	0.93*
Pre-chamber fuel-air equivalence ratio (ϕ_{PC})	1.08*
Natural gas fumigation injection DSE [µs]	15878 - 11062
Main-chamber air-fuel ratio (λ_{MC})	1.7, 1.8, 19, 2.0, 2.2, 2.4, 2.6
Main-chamber fuel-air equivalence ratio (ϕ_{MC})	0.59, 0.56, 0.53, 0.50, 0.45, 0.42, 0.38

Table 2. Experimental conditions and test case specifications.

The optical engine is operated in a "9:1 skip-fire" mode to avoid excessive temperature gradients within the optical windows that could cause damage. That is, nine motored cycles precede each fired cycle. As a result of continuous gas-exchange, the skip-fire operation minimizes the amount of residual gases present inside the pre-chamber and the main-chamber clearance volume. This allows for a fundamental study of the physical processes governing the pre-chamber spark ignition system avoiding any residual gas effects. Each experimental test run consists of 54 fired cycles after the engine is motored for 60 seconds at a constant speed of 1200 rotations per minute (RPM). The salient operating conditions of the engine and the test matrix are tabulated in Table 2. The pre-chamber spark timing is held constant for all experiments at 343 CAD, with 360 CAD defined as top dead-center (TDC) of the compression stroke.

As specified in Table 2, two different pre-chamber fueling configurations are studied: (i) pre-chamber only fueling ($\lambda_{PC} = 0.93$), i.e., no natural gas in the main-chamber (natural gas fumigation injector is disabled), and (ii) fueled pre-chamber, i.e., main-chamber is fumigated with natural gas; main-chamber air-fuel ratio (λ_{MC}) is varied between 1.7 and 2.6 for a fixed pre-chamber air-fuel ratio ($\lambda_{PC} = 0.93$). This value $\lambda_{PC} = 0.93$ was chosen based on other experimental sweeps (not shown in this work), where the pre-chamber air-fuel ratio (λ_{PC}) was varied between 1.65 and 0.5 for a fixed main-chamber air-fuel ratio ($\lambda_{MC} = 1.65$). $\lambda_{PC} = 0.93$ exhibited stable combustion (no misfires, COV of IMEP < 5%) with the highest rate of pressure rise at fixed spark timing and end of solenoid energization.

3. Results and Discussion

3.1. Pre-chamber only fueling experiments with no natural gas in main-chamber

To isolate and characterize the evolution of the pre-chamber jets in the absence of natural gas in the main-chamber, pre-chamber only fueling experiments were carried out by disabling the natural gas fumigation injector. To achieve the targeted pre-chamber air-fuel ratio ($\lambda_{PC} = 0.93$), the calibrated pre-chamber injector delivers a specified quantity of natural gas (SSE = 325.75 CAD; DSE = 1517 µs; ESE = 336.5 CAD) into the pre-chamber. This is then followed by pre-chamber spark ignition at 343 CAD, resulting in combustion of the pre-chamber charge causing a subsequent increase in its pressure and temperature, which results in the forceful ejection of the pre-chamber gases in the form of "jets" into the main-chamber. Thus, the pressure difference between the pre-chamber and the main-chamber acts as the primary driving force for the formation of the pre-chamber jets and its subsequent mixing with the contents of the main-chamber.

3.1.1. Pre-chamber jet development

The pre-chamber pressure, main-chamber pressure, and the corresponding pressure difference for pre-chamber only fueling are shown in Figure 2.(a), 2.(b) and 2.(c), respectively. The dark green pressure trace is the ensemble-averaged result of the 54 individual fired cycle pressure traces shown in light green. The ensemble-averaged motored cycle pressure trace is also shown in black for reference. Even in the absence of combustion, based on a comparative analysis of the motored cycle pre-chamber and main-chamber pressure traces (not shown here), a clear lag in pressure-equilibration is observed. Despite continuous gas-exchange and no combustion, there is a non-zero pressure difference between the pre-chamber and the main-chamber throughout the majority of the compression ($P_{MC} > P_{PC}$, $\Delta P_{max} \sim$ -0.26 bar @ 340 CAD) and expansion ($P_{PC} > P_{MC}$, $\Delta P_{max} \sim$ 0.43 bar @ 381.5 CAD) strokes with reversal at around 360 CAD (TDC).
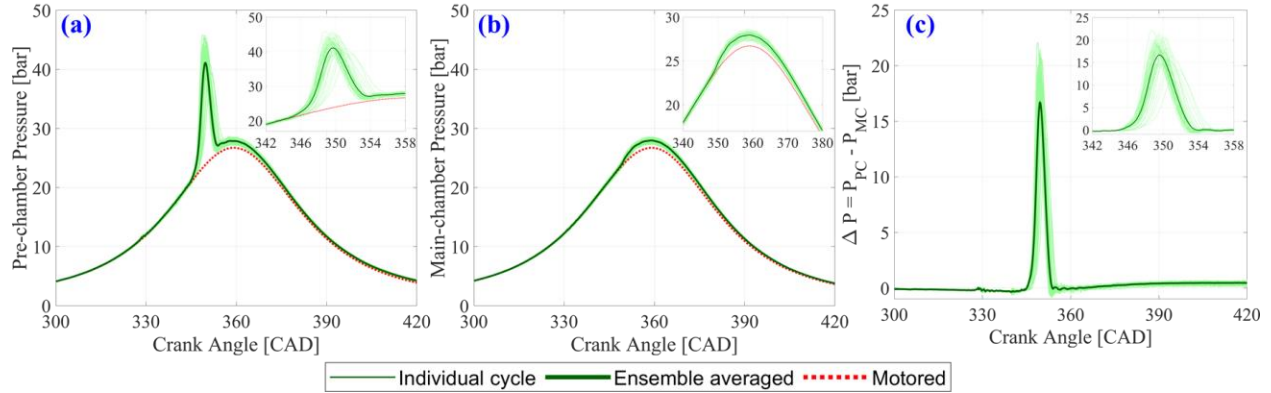
Figure 2. (a) Pre-chamber pressure. (b) Main-chamber pressure. (c) Pressure difference between the pre-chamber and main-chamber for pre-chamber only fueling experiments. Fueling parameters: SSE = 325.75 CAD, DSE = 1517 µs, ESE = 336.5 CAD, λ_{PC} = 0.93. No natural gas in the main-chamber. Inlay plots show zoomed-in trends in the region of interest. The individual 54 fired cycles are shown in a lighter color shade with the corresponding darker color shade indicating the ensemble-averaged results.

The individual pressure traces show clear indication of cycle-to-cycle variability both in terms of magnitude and corresponding CAD timing. Within 2.5 - 4.5 CAD after the pre-chamber spark ignition, there is a clear increase in the pre-chamber pressure due to combustion as indicated by the rapid increase in the pressure-difference ($\Delta P > 0.5$ bar) between the pre-chamber and the main-chamber. Based on the ensemble averaged data, the pre-chamber pressure rises ($\Delta P > 0.5$ bar) rapidly after 346 CAD and reaches a maximum of 41.11 bar at 349.5 CAD, which corresponds to a maximum pressure difference of 16.71 bar between the pre-chamber and main-chamber. Due to the absence of natural gas in the main-chamber, there is only a marginal increase in its pressure due to pre-chamber combustion, i.e., the maximum main-chamber pressure exceeds the corresponding motored pressure by less than 1.2 bar. Furthermore, due to the relatively meager quantity of fuel injected in the pre-chamber, the pressure difference between the pre-chamber and the main-chamber drops back to near zero levels rapidly in a coincidentally symmetric fashion by 353.25 CAD. In terms of cycle-to-cycle variation, the maximum pressure difference between the pre-chamber and the main-chamber ranges between 22.13 bar and 13.49 bar (COV ~ 10.72%),

while the corresponding CAD timing ranges from 348.75 - 351.75 CAD. This variation is most likely due to a combination of intense turbulence induced stratification of the pre-chamber charge caused by the fuel injection event and the non-uniformities in the flame kernel development inside the pre-chamber [30] which in turn affects the rate and timing of pressure increase within the pre-chamber.

3.1.2. Composite infrared and broadband chemiluminescence imaging

Figure 3 shows a montage comprising of selected composite snapshots from key timings for pre-chamber only fueling experiments. These composite snapshots were created by carefully superimposing simultaneously acquired infrared images (employing a red color map) and broadband chemiluminescence images (employing a green color map). This allows for distinguishing between regions of burnt gases (stronger IR emission from combustion products at high temperature) and active chemical reactions (stronger chemiluminescence emission from combustion intermediates), respectively, while describing the overall spatial and temporal evolution of the pre-chamber jets. Due to the selected color scheme, regions of overlap between infrared and broadband chemiluminescence activity appears in shades of yellow. To account for differences in the resolution and the field of view between the two cameras used in this study, a MATLAB-based geometric image transformation is used to align the two images required to create the composite snapshot. This is done by identifying selective control points such as points on the piston window boundary and the center of the pre-chamber in each pair of image that are then mapped onto one another to correlate the two images for creating the composite snapshot. The acquisition CAD and acquisition cycle are also indicated on the top-left and bottom-left corner of each image, respectively. It is to be noted that though the infrared and broadband chemiluminescence images in any single snapshot were acquired simultaneously, the selected

series of snapshots presented in Figure 3 are, however, non-sequential, i.e., each composite image belongs to a different acquisition cycle. This is due to the disparity in the framing rates between the two cameras used in this study, i.e., for every fired cycle, the infrared camera acquires one image at a specified CAD, while the high-speed camera acquires a series of images every 0.25 CAD.
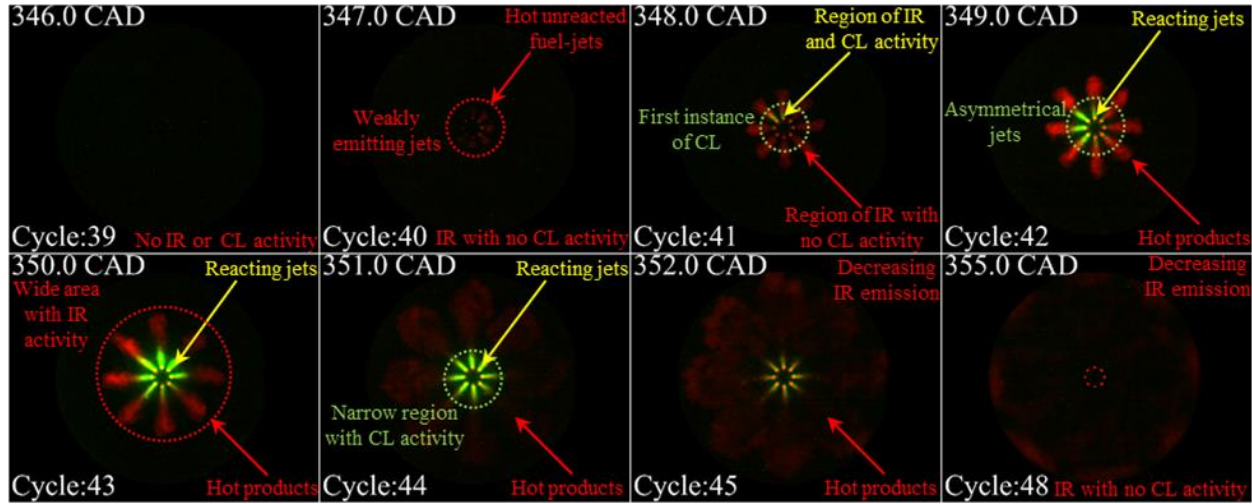

Figure 3. Composite snapshots consisting of infrared images (red) overlaid on broadband chemiluminescence images (green) for pre-chamber only fueling experiments. Acquisition CAD and acquisition cycle are indicated on the top-left and bottom-left corner of each image respectively. Fueling parameters: SSE = 325.75 CAD, DSE = 1517 μs, ESE = 336.5 CAD, λ_{PC} = 0.93. No natural gas in the main-chamber.

At 346 CAD, although there is a slight pressure rise in the pre-chamber (ΔP ~ 0.73 bar) indicating a developing ignition-kernel flame-front inside the pre-chamber, there is no discernible infrared or chemiluminescence emission that is observable. However, as the flame-front continues to propagate and consumes through the pre-chamber mixture, the initial pressure rise in the pre-chamber (ΔP ~ 2.34 bar) forces hot-unreacted fuel-air mixture situated near the orifices into the main-chamber [34, 48, 49] in the form of weakly emitting, pre-chamber jets, which are starting to appear at 347 CAD. The first appearance of broadband chemiluminescence at 348 CAD (ΔP ~ 6.45 bar) along with increasing infrared emission from the pre-chamber jets signifies the

arrival of the propagating flame front at the pre-chamber nozzles. Thus structurally at this point, the pre-chamber jets are composed of a still reactive jet that is followed by hot products of combustion from the pre-chamber, and fresh unreacted fuel-air mixture that was ejected first as the pre-chamber pressure initially began to rise [34]. The schematic shown in Figure 4 elucidates this phase of development of the pre-chamber jets just as they begin to emerge from the pre-chamber and continue to penetrate further into the main-chamber along with its spatial structure. As explained earlier in Figure 2, the pre-chamber pressure then rapidly increases, reaches a maximum and then quickly decays between 349 - 352 CAD (ΔP_{max} ~ 16.97 bar). This interval is marked by narrow regions of intense broadband chemiluminescence localized to the pre-chamber periphery that overlaps (shown in yellow) with the infrared signal. Further, there is no evidence of the unreacted fuel-air mixture, which was ejected out into the main-chamber initially, igniting and undergoing combustion, as chemiluminescence tends to stays near the nozzle and does not propagate temporarily into the pre-existing unburned jet. Quantification of the local mixing using a 1-D jet model suggests a strong dilution effect i.e., the ejected pre-chamber flow is highly diluted by the main-chamber air due to intense mixing, leading to the formation of a fuel-air mixture that is too lean to react. However, the hot products of combustion, which now primarily constitute the pre-chamber jets, continue to further penetrate and reach the bowl wall by 351 CAD as indicated by the infrared signal that is now distributed over a wide region. This is the first indication of the importance of mixing process on subsequent combustion development.

The pre-chamber jets also exhibit a clear spatial (distribution) and temporal (timing) asymmetry in terms of both the infrared and broadband chemiluminescence signal levels as highlighted in Figure 3. This observed asymmetry is most likely due to the combination of intense turbulence-induced stratification of the pre-chamber charge caused by the fuel injection event and

the stochastic nature of the ignition event. These effects combined might lead to non-uniformities in the shape and direction of the initial flame-kernel development inside the pre-chamber [30] (as highlighted in Figure 4) that play a key role in determining the order in which the pre-chamber orifices discharges, which would partly contribute to the observed cycle-to-cycle variation highlighted in Figure 2. By 355 CAD, there is negligible driving force ($\Delta P < 0.1$ bar) behind the pre-chamber jets signifying the end of combustion. This is marked by no observable chemiluminescence activity along with diffused, decreasing infrared emission that is distributed throughout the main-chamber, which is most likely due to the mixing of hot combustion products from the pre-chamber with cooler surrounding air from the main-chamber.
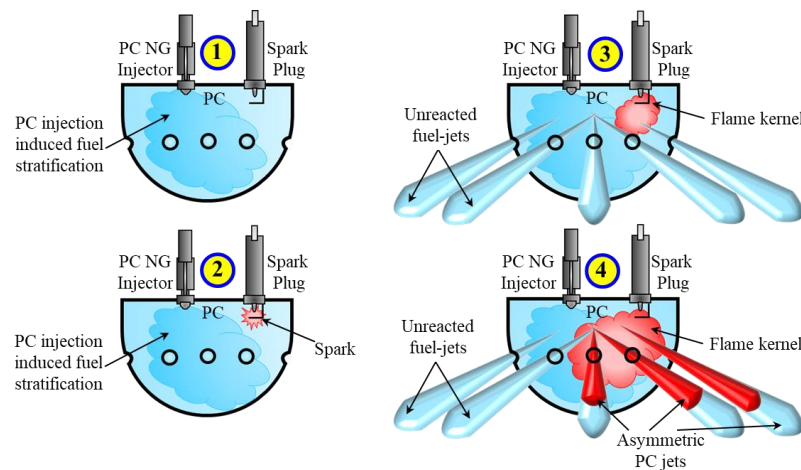

Figure 4. Schematic illustrating the evolution of combustion process in the pre-chamber and the subsequent development of spatial and temporal asymmetries in pre-chamber jets due to fuel stratification and non-uniformities in flame kernel development within the pre-chamber.

3.2. Fueled pre-chamber experiments with premixed natural gas charge in main-chamber

Combustion of the pre-chamber charge results in the formation of pre-chamber jets, which then serve as a distributed ignition source for the main-chamber gases. As the pre-chamber jets emerge, they continue to mix with and ignite the main-chamber charge, thereby driving the progression of main-chamber combustion, whether by flame propagation or sequential

auto-ignition. In the fueled pre-chamber experiments, the pre-chamber air-fuel ratio is held constant (λ_{PC} = 0.93) while the main-chamber air-fuel ratio (λ_{MC}) is varied between 1.7 to 2.6 to characterize the effect of active fueling on the ignition characteristics, combustion mode (flame propagation / sequential auto-ignition), lean limits, and cycle-to-cycle variability. The pre-chamber injector's end of solenoid energization timing (ESE = 336.5 CAD) and the spark timing (343 CAD) were held constant throughout the experiments. However, despite the pre-chamber air-fuel ratio being held constant, the pre-chamber injection duration (DSE) and thus the SSE had to be suitably adjusted. This was to account for the varying composition of the initial premixed charge inside the pre-chamber (due to gas-exchange) before fuel injection as the main-chamber charge composition was varied. Since the skip-fire operation allows for continuous gas-exchange, the amount of residual gases present inside the pre-chamber and the main-chamber clearance volume is therefore minimized, thereby effectively avoiding the influence of residual gases on the ignition process in subsequent fired cycles.

3.2.1. Penetration characteristics of pre-chamber jets

The pre-chamber pressure, main-chamber pressure, and the corresponding pressure difference for fueled pre-chamber tests are shown Figure 5.(a), 5.(b), and 5.(c), respectively. The dark colored pressure trace is the ensemble-averaged result of the 54 individual fired cycle pressure traces shown in corresponding lighter color shade. The ensemble averaged motored cycle pressure trace is also shown in black for reference. For ease of comparison, the corresponding ensemble-averaged maximum values of the pre-chamber pressure, the main-chamber pressure, and the associated pressure difference for fueled pre-chamber tests are shown in Figure 6, with Figure 6.(a) and 6.(b) indicating the corresponding cycle-to-cycle variations in the form of error bars and individual data points from all 54 fired cycles, respectively.

Despite the pressure-difference between the pre-chamber and the main-chamber exhibiting almost similar levels of cycle-to-cycle variability (COV ~ 16%) as described in the pre-chamber only fueling case (COV ~ 11%), Figure 5 and 6 clearly show that the maximum pressure difference and thus the maximum pre-chamber pressure during the pre-chamber combustion phase is almost independent of the main-chamber charge composition (λ_{MC}). Based on the ensemble averaged values, the maximum pressure difference and the corresponding maximum pre-chamber pressure during the pre-chamber combustion phase are 13.18 bar (COV ~ 3.85%) and 38.15 bar (COV ~ 1.39%), respectively, for varying main-chamber charge composition, which is well within their corresponding cycle-to-cycle variation of ~16% and ~6% respectively. This ensemble averaged maximum pressure difference is ~20% lower when compared to the pre-chamber only fueling data presented in Figure 2, though the reason for this observed decrease is rather unclear at this point. This shows that the driving force, i.e., the pressure difference between the pre-chamber and the main-chamber, which provides momentum to the pre-chamber jets and thereby governs its development, formation, and mixing characteristics, remains the same (independent of λ_{MC}) as it is mostly controlled by the pre-chamber air-fuel ratio (λ_{PC}) that is held constant throughout. However, as expected, Figure 6 shows a clear linear dependence of maximum main-chamber pressure on its operating air-fuel ratio (λ_{MC}) (max P_{MC} ~ 58.31 bar for $\lambda_{MC} = 1.7$; max P_{MC} ~ 39.25 bar for $\lambda_{MC} = 2.6$) with individual cycle-to-cycle COVs not exceeding 3.68%.
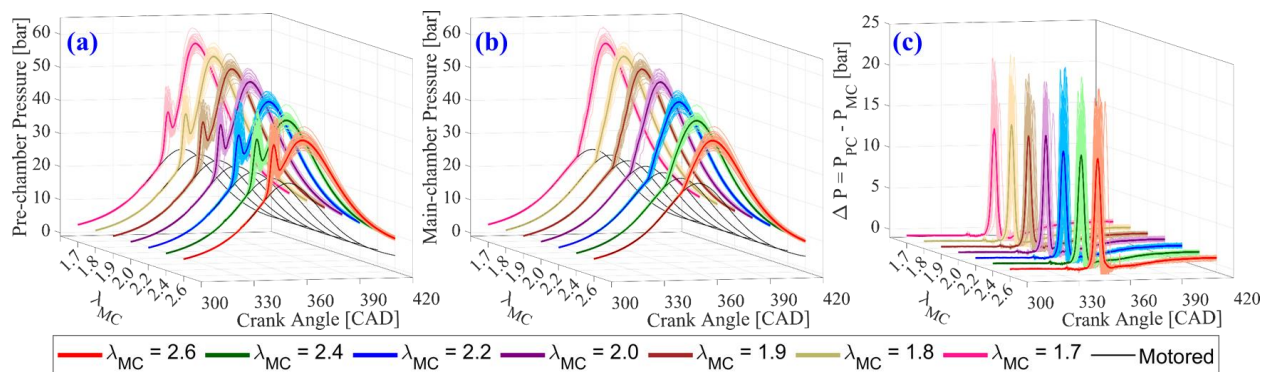
Figure 5. (a) Pre-chamber pressure. (b) Main-chamber pressure. (c) Pressure difference between the pre-chamber and main-chamber for fueled pre-chamber experiments. λ_{PC} is held constant at 0.93 for varying λ_{MC}. The individual 54 fired cycles are shown in a lighter color shade with the corresponding darker color shade indicating the ensemble averaged results.
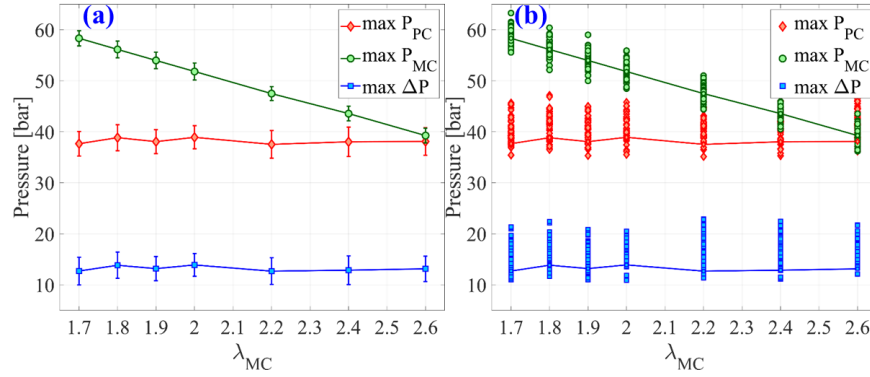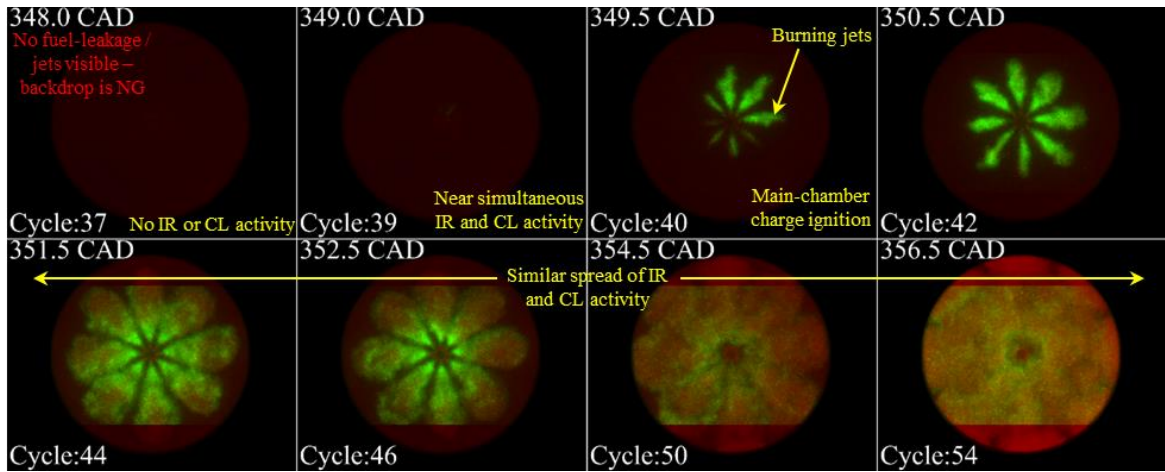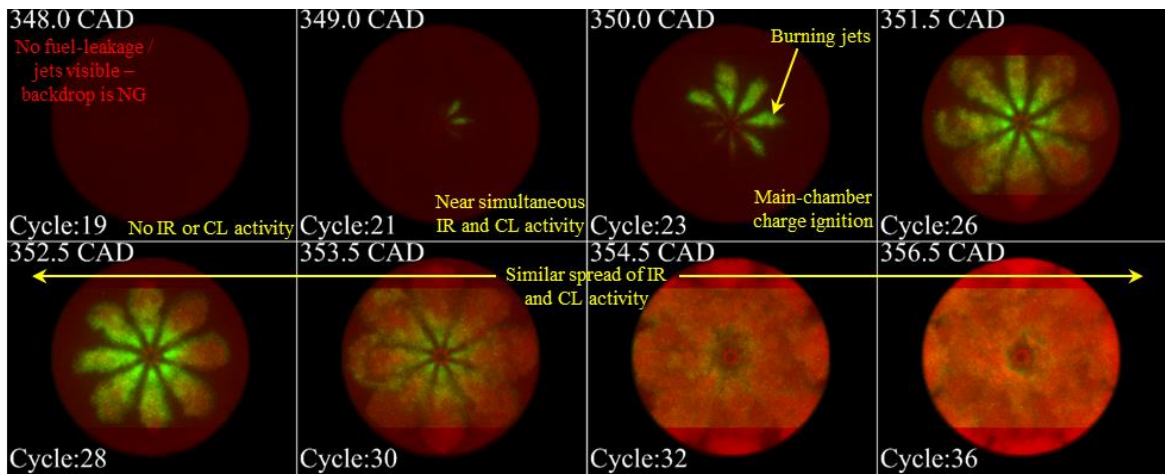

Figure 6. Ensemble-averaged maximum values of pressure difference, pre-chamber pressure (during the pre-chamber combustion phase), and main-chamber pressure for various λ_{MC} for fueled pre-chamber experiments. (a) Error bars indicate two standard deviations of cycle-to-cycle variations. (b) Individual data points from all 54 fired cycles. λ_{PC} is held constant at 0.93 for varying λ_{MC}.

The composite snapshots presented in Figure 7 are identical to the ones presented in Figure 3, except that the new montages are composed of OH* chemiluminescence images (employing a green color map) in place of broadband chemiluminescence images that were used earlier. Figure 7.(a) through 7.(f) show individual montages comprising of selected composite infrared and OH* chemiluminescence snapshots from key timings for fueled pre-chamber experiments as the main-chamber air-fuel ratio (λ_{MC}) is varied between 1.7 and 2.6 for a fixed pre-chamber air-fuel ratio ($\lambda_{PC} = 0.93$). The corresponding acquisition CAD and acquisition cycle are also indicated on the top-left and bottom-left corner of each image, respectively. While the entire piston bowl is fully captured within the field of view of the infrared camera, the field of view of the high-speed (chemiluminescence) camera is restricted to only around 75% of the total height of the piston bowl in the vertical direction.
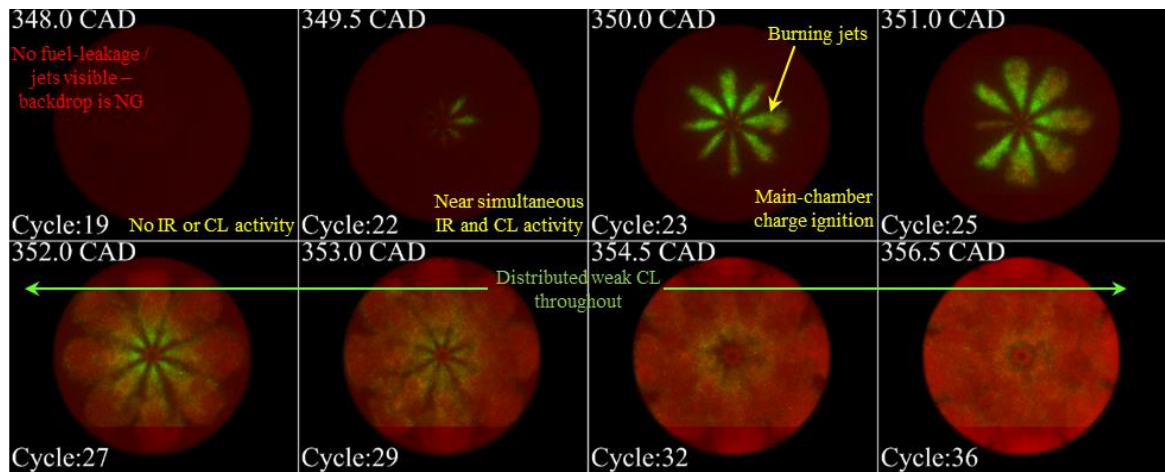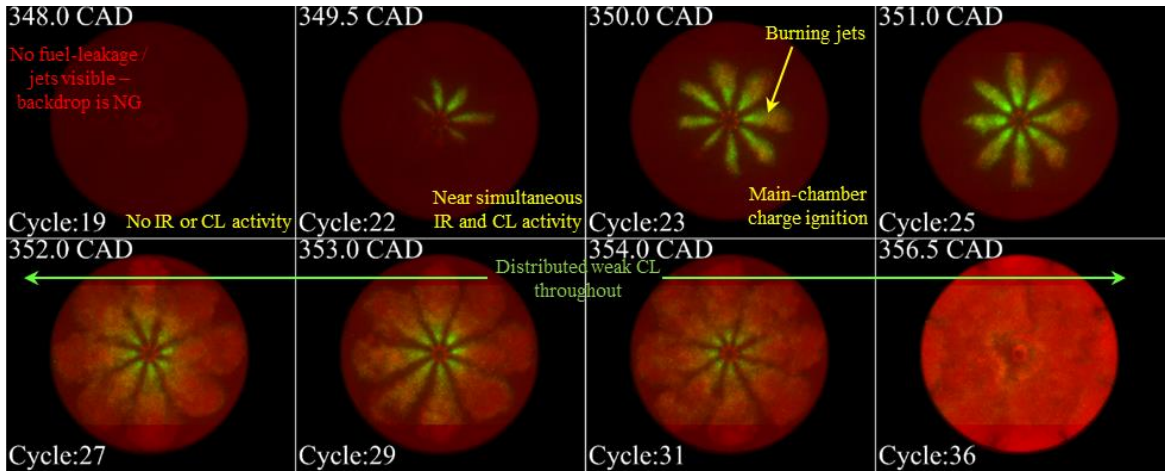
(a) $\lambda_{MC} = 1.7$

348.0 CAD
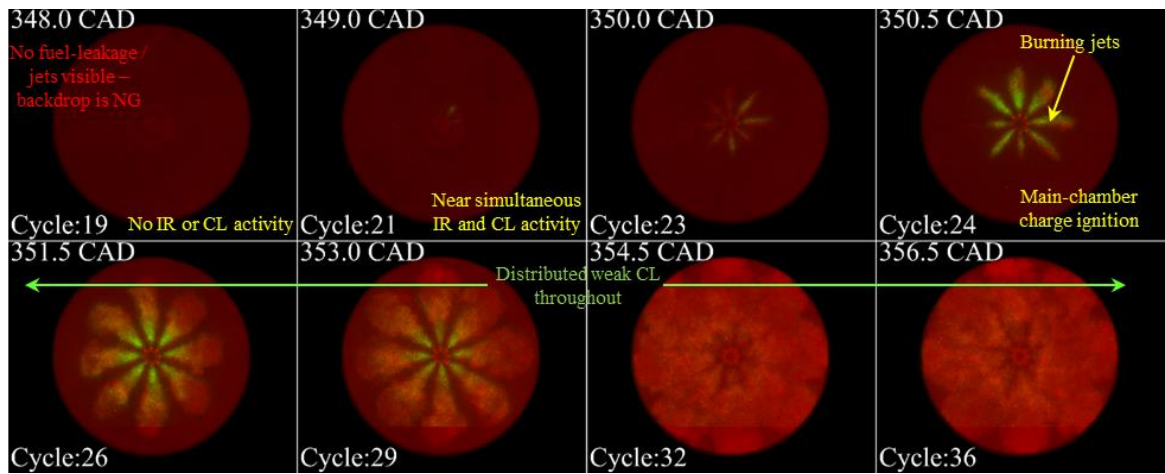No fuel-leakage / jets visible – backdrop is NG
Cycle:37 — No IR or CL activity

349.0 CAD
Cycle:39 — Near simultaneous IR and CL activity

349.5 CAD
Burning jets
Cycle:40 — Main-chamber charge ignition

350.5 CAD
Cycle:42

351.5 CAD
Similar spread of IR and CL activity
Cycle:44

352.5 CAD
Cycle:46

354.5 CAD
Cycle:50

356.5 CAD
Cycle:54

(b) $\lambda_{MC} = 1.8$

348.0 CAD
No fuel-leakage / jets visible – backdrop is NG
Cycle:19 — No IR or CL activity

349.0 CAD
Cycle:21 — Near simultaneous IR and CL activity

350.0 CAD
Burning jets
Cycle:23 — Main-chamber charge ignition

351.5 CAD
Cycle:26

352.5 CAD
Similar spread of IR and CL activity
Cycle:28

353.5 CAD
Cycle:30

354.5 CAD
Cycle:32

356.5 CAD
Cycle:36

(c) $\lambda_{MC} = 1.9$

348.0 CAD
No fuel-leakage / jets visible – backdrop is NG
Cycle:19 — No IR or CL activity

349.5 CAD
Cycle:22 — Near simultaneous IR and CL activity

350.0 CAD
Burning jets
Cycle:23 — Main-chamber charge ignition

351.0 CAD
Cycle:25

352.0 CAD
Distributed weak CL throughout
Cycle:27

353.0 CAD
Cycle:29

354.5 CAD
Cycle:32

356.5 CAD
Cycle:36

(d) $\lambda_{MC} = 2.0$

348.0 CAD	349.5 CAD	350.0 CAD	351.0 CAD
No fuel-leakage / jets visible – backdrop is NG		Burning jets	
Cycle:19 No IR or CL activity	Cycle:22 Near simultaneous IR and CL activity	Cycle:23 Main-chamber charge ignition	Cycle:25

352.0 CAD	353.0 CAD	354.0 CAD	356.5 CAD
		Distributed weak CL throughout	
Cycle:27	Cycle:29	Cycle:31	Cycle:36

(e) $\lambda_{MC} = 2.2$

348.0 CAD	349.0 CAD	350.0 CAD	350.5 CAD
No fuel-leakage / jets visible – backdrop is NG			Burning jets
Cycle:19 No IR or CL activity	Cycle:21 Near simultaneous IR and CL activity	Cycle:23	Cycle:24 Main-chamber charge ignition

351.5 CAD	353.0 CAD	354.5 CAD	356.5 CAD
		Distributed weak CL throughout	
Cycle:26	Cycle:29	Cycle:32	Cycle:36

(f) $\lambda_{MC} = 2.4$

348.0 CAD	350.5 CAD	351.0 CAD	351.5 CAD
No fuel-leakage / jets visible – backdrop is NG		Burning jets	
Cycle:19 No IR or CL activity	Cycle:24 Near simultaneous IR and CL activity	Cycle:25	Cycle:26 Main-chamber charge ignition

352.0 CAD	353.0 CAD	354.0 CAD	356.5 CAD
		Distributed weak CL throughout	
Cycle:27	Cycle:29	Cycle:31	Cycle:36

Figure 7. Composite snapshots consisting of infrared images (red) overlaid on OH* chemiluminescence images (green) for fueled pre-chamber experiments. Acquisition CAD and acquisition cycle are indicated on the top-left and bottom-left corner of each image respectively. λ_{PC} is held constant at 0.93 for varying λ_{MC} (a) 1.7 (b) 1.8 (c) 1.9 (d) 2.0 (e) 2.2 (f) 2.4 (g) 2.6.

Unlike the pre-chamber only fueling montage presented earlier in Figure 3, the ejection of hot, unreacted fuel-air mixture near the orifices in the form of jets due the initial pressure rise in the pre-chamber is not easily discernible from the series of montages presented in Figure 7. This is most likely due to the infrared signature of the hot-unreacted fuel-air mixture, pushed out from the pre-chamber, being indistinguishable from the fairly uniform, background infrared emission signal of the natural gas that is already present inside the main-chamber. Thus, pre-chamber jets with near simultaneous appearance of infrared and OH* chemiluminescence signals (marked by overlap regions shown in yellow) that signify the arrival of the propagating flame front at the pre-chamber nozzles are observed at around 349.5 CAD ($\Delta P \sim 3$ bar), irrespective of the main-chamber charge composition (λ_{MC}). This further supports the expectation that the driving force, i.e., the pressure difference, which governs the development, formation, and mixing characteristics of the pre-chamber jets, is most likely controlled by the pre-chamber air-fuel ratio (λ_{PC}) that is held constant throughout as explained in the previous section. In the initial phase of development, as the pre-chamber jets emerge, they do exhibit clear spatial (distribution) and temporal (timing)

asymmetry, most likely due to the turbulence induced fuel-stratification and non-uniform flame kernel development inside the pre-chamber [30]. This is then followed by the near instantaneous ignition (within 1 CAD, ~ 350 CAD) of the main-chamber charge, as indicated by the spread of the OH* chemiluminescence signal in the axial direction beyond the periphery of the pre-chamber indicating the onset of chemical reactions in the main-chamber. The initially observed spatial and temporal asymmetry in the pre-chamber jets is however quickly lost, i.e., as they continue to develop, the pre-chamber jets tend to be become fairly symmetrical by the time they reach the bowl wall. This is at least in part due to the homogeneity of the main-chamber charge, which at least in part counteracts the stratification inside the pre-chamber that resulted in the initial asymmetry of the pre-chamber jets. There is also a noticeable spread of the pre-chamber jets in the azimuthal direction (increasing jet width) as it continues to penetrate further and reach the bowl wall around 354 CAD, with a near identical spread (overlap) of OH* chemiluminescence and infrared emission throughout the entire process. This observed spread is at least in part due to the pre-chamber jets functioning as a distributed surface ignition source for the surrounding natural gas charge. This might also be due to the enhanced mixing effects as the pressure difference between the pre-chamber and main-chamber continues to drop, akin to the end of injection entrainment event observed in diesel-jets [50]. Further, the intensities of both OH* chemiluminescence and infrared emission decrease with decreasing natural gas concentration in the main-chamber. This is most likely due to increasingly lean mixtures in the main-chamber leading to lower heat release and reduced adiabatic flame temperatures, resulting in lower OH* concentrations.
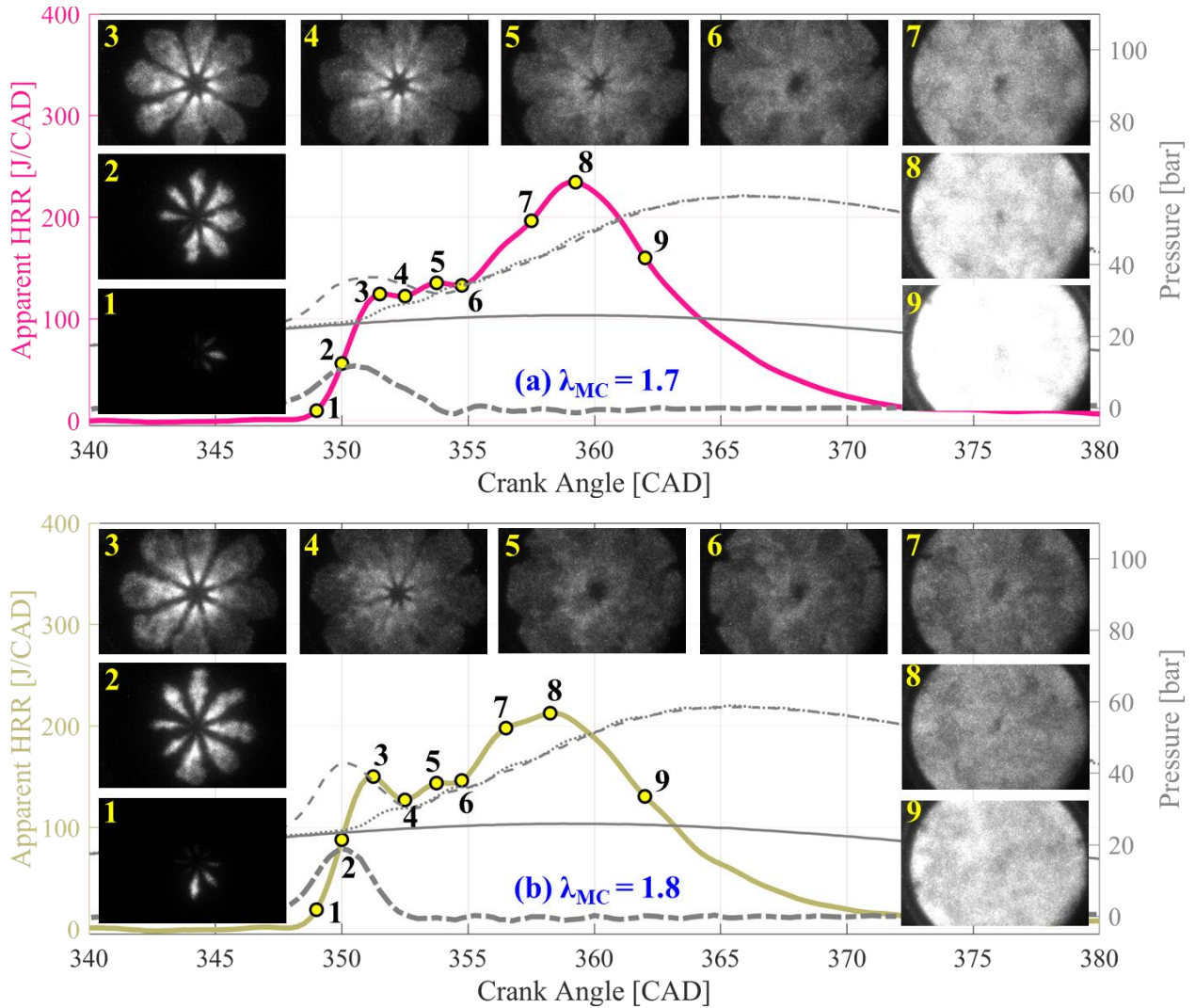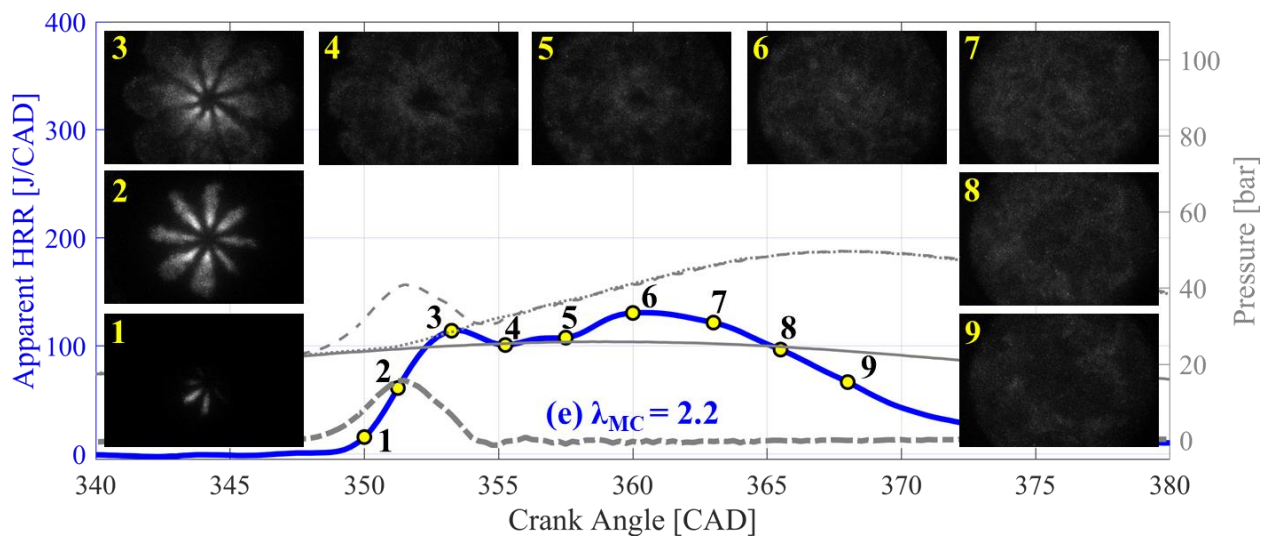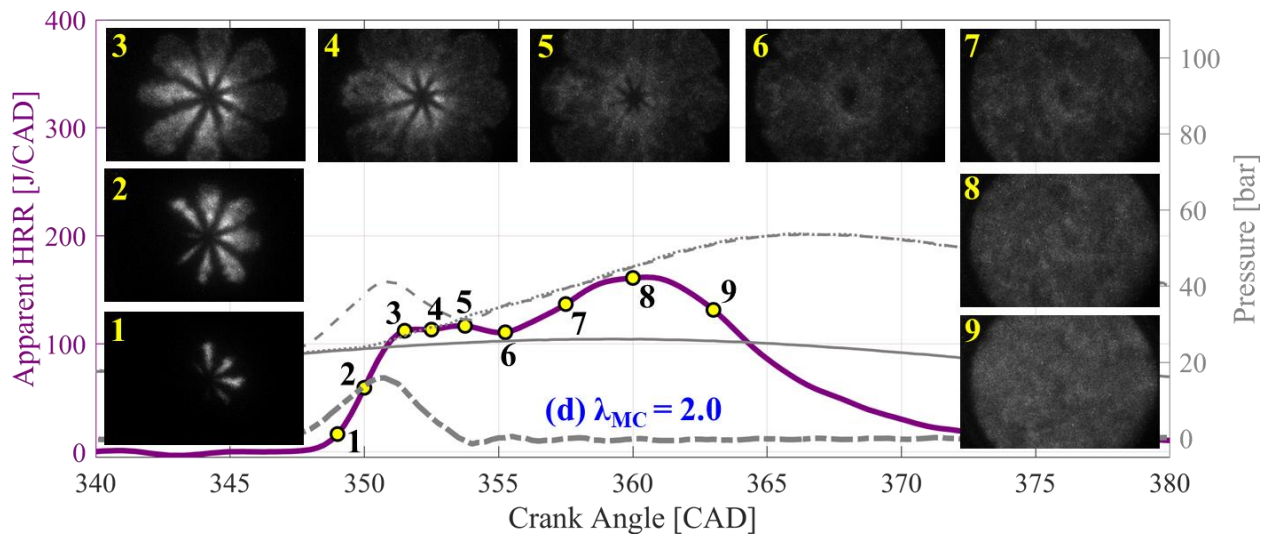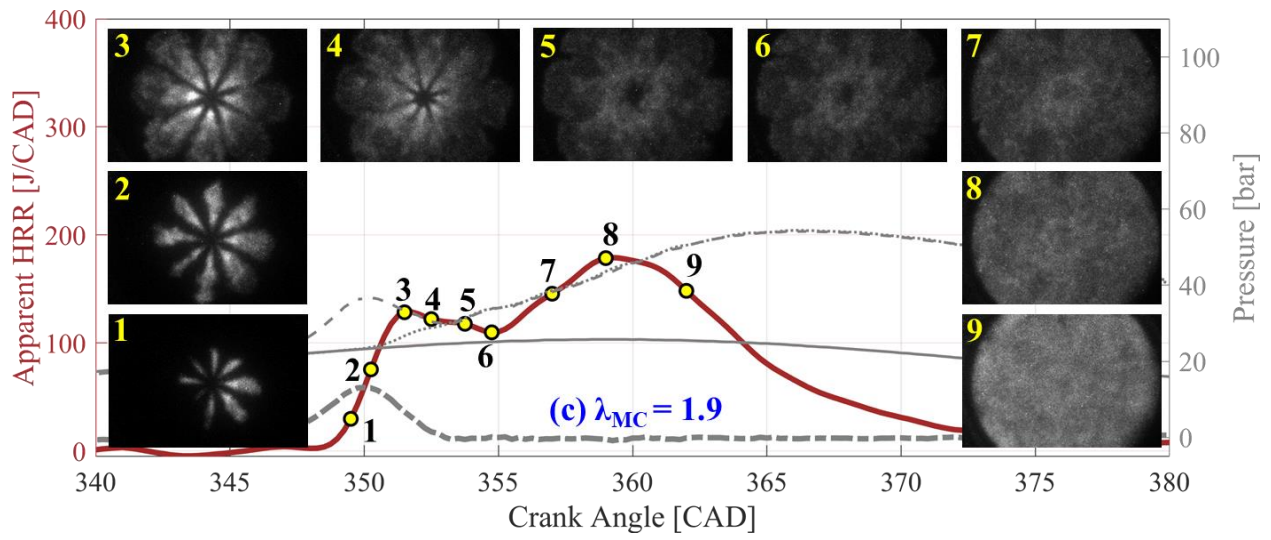
3.2.2. Two-staged apparent heat release rate

Figure 8.(a) through 8.(f) are a compilation of summary plots comprising of the apparent

heat release rate (AHRR) along with relevant pressure traces (main-chamber pressure, pre-chamber pressure, and corresponding pressure difference) from a representative individual fired cycle for fueled pre-chamber experiments, as the main-chamber air-fuel ratio (λ_{MC}) is varied between 1.7 and 2.6 for a fixed pre-chamber air-fuel ratio (λ_{PC} = 0.93). The ensemble averaged motored cycle pressure trace is also shown for reference. The series of images that are embedded in each of the summary plots are snapshots of sequential OH* chemiluminescence images that were captured at key timings as identified by the image labels (1-9) corresponding to identical labels on the AHRR curve. Image labels 1 through 3 signify key timings corresponding to the first instance of AHRR exceeding 5 J/CAD, the pressure difference between pre-chamber and main-chamber is maximum, and the AHRR is at its first local maximum, respectively. Image labels 4 through 9 signify key timings characterized by either a local minimum, a local maximum, or a inflection point in the AHRR. It is to be noted that these OH* chemiluminescence images are line of sight measurements with the resulting 2D-image being representative of integrated volumetric chemiluminescence across the depth of the entire combustion chamber. The scales for AHRR (on the left Y-axis) and the pressure trace (on the right Y-axis) along with the color scale for the OH* chemiluminescence images are kept consistent throughout the summary plots for ease of comparison between the test cases.

Figure 8.(a) through 8.(f) clearly exhibit near identical trends in both magnitude and timing of the pre-chamber pressure rise (through the pre-chamber combustion phase) and the corresponding pressure difference between the pre-chamber and main-chamber that remain independent of the main-chamber charge composition (λ_{MC}). The minor variations observed in these trends are well within their corresponding cycle-to-cycle variations quantified earlier. Thus, it is clear that the pressure difference between the pre-chamber and the main-chamber, which

functions as the primary driving force that governs the formation, development, and mixing characteristics of the pre-chamber jets, remains similar as its magnitude and timing is solely determined by the air-fuel ratio in the pre-chamber (λ_{PC}), which is held constant throughout. However, the maximum main-chamber pressure increases linearly with increasing natural gas concentration in the main-chamber as shown in Figure 5.
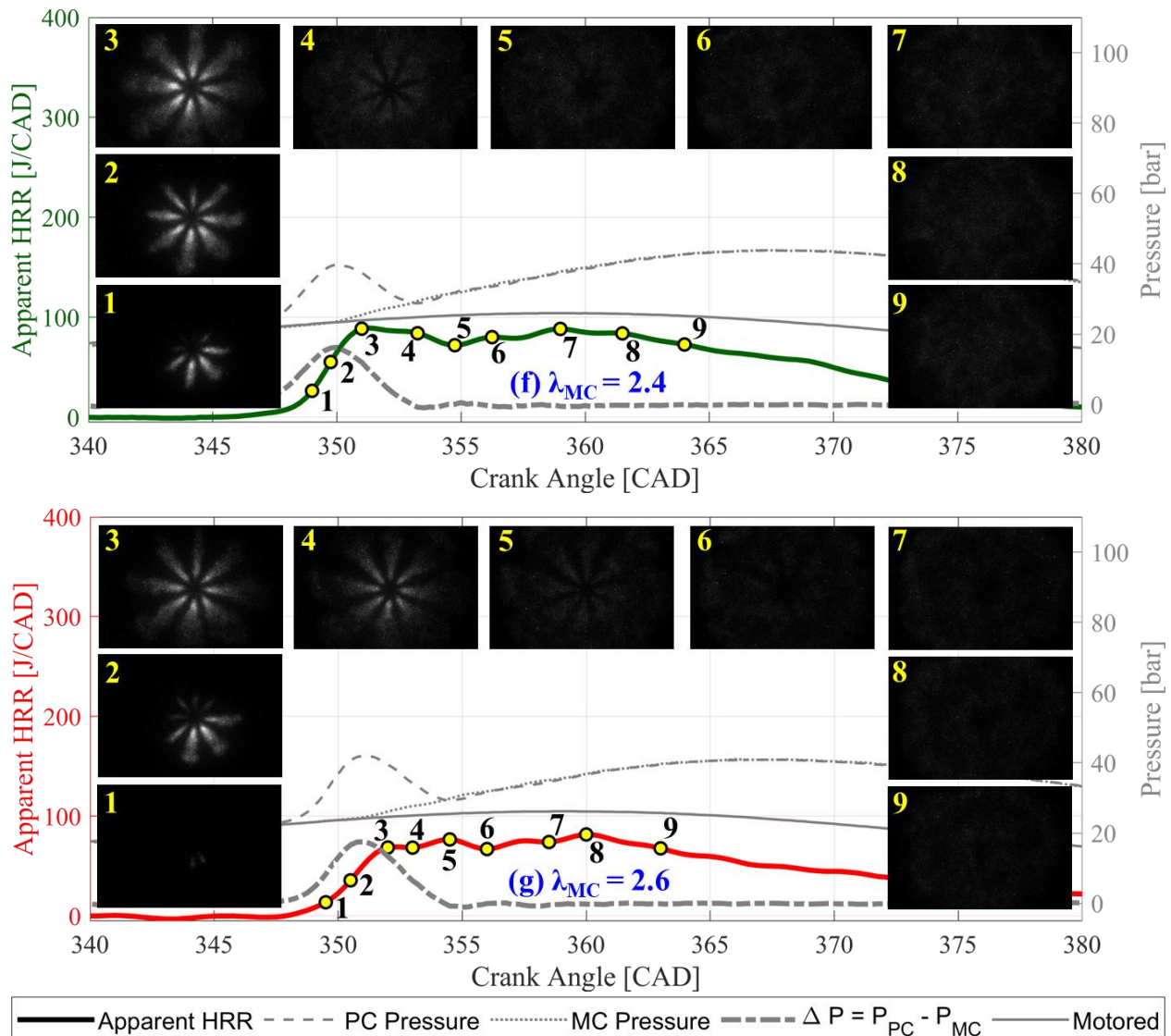
(c) $\lambda_{MC} = 1.9$

(d) $\lambda_{MC} = 2.0$

(e) $\lambda_{MC} = 2.2$

Figure 8. Apparent heat release rate along with main-chamber pressure, pre-chamber pressure, pressure difference, and motored pressure from a single representative cycle for fueled pre-chamber experiments. Embedded in the plots are OH* chemiluminescence images captured at key timings as identified by the image labels (1-9) corresponding to similar labels on the AHRR curve. λ_{PC} is held constant at 0.93 for varying λ_{MC} (a) 1.7 (b) 1.8 (c) 1.9 (d) 2.0 (e) 2.2 (f) 2.4 (g) 2.6.

The AHRR release rates do tend to exhibit some remarkably similar trends despite the wide range of air-fuel ratio inside the main-chamber. The start of combustion (AHRR exceeding 5 J/CAD) in the main-chamber is consistently around 349 CAD, which is also coincident with the appearance of chemically reactive pre-chamber jets (image label: 1) that function as a distributed

ignition source for the main-chamber charge. It is to be noted that the marginal increase in AHRR observable around 345 to 348 CAD is mostly likely due to the consumption of natural gas charge contained within the pre-chamber as there is no discernible pressure rise in the main-chamber, i.e., the main-chamber pressure is identical to the motoring pressure until 350 CAD. As the AHRR continues to increase, the pressure difference between the pre-chamber and the main-chamber reaches its maximum value, which is characterized by pre-chamber jets continuing to spread azimuthally as they penetrate further radially into the main-chamber, with a few or all of the pre-chamber jets reaching the bowl wall (image label: 2). During this phase of development of the pre-chamber jets (images: 1-2), the continuously increasing flame surface area, i.e., the turbulent periphery of the jet, also increases the number of reaction sites that allows for faster consumption of the main-chamber charge in between the pre-chamber jets, thereby leading to an increase in the AHRR. Moreover, the pre-chamber jets also exhibit clear signs of asymmetry, most likely due to turbulence-induced fuel-stratification and non-uniform flame kernel development inside the pre-chamber [30] due to the stochastic nature of the associated spark ignition.

The AHRR profile exhibits a clear two-staged heat release feature throughout. A first peak in AHRR (local maximum) is followed by a period of sustained drop in AHRR resulting in a local minimum (dip), beyond which there is an increase in AHRR resulting in a second peak (generally the global maximum), whose magnitude decreases with decreasing natural gas concentration in the main-chamber. The first peak in AHRR around 353 CAD is characterized by the presence of fairly uniform, pre-chamber jets that are fully emerged (ΔP at near zero levels) and yet individually distinguishable, i.e., at the verge of merging (image label: 3). Any asymmetry that was present in the earlier stages of the pre-chamber jet development is no longer obvious, with all the pre-chamber jets tending to be fairly symmetrical by the time they reach the bowl wall. This is at least in part

due to the homogeneity of the main-chamber charge that counteracts the stratification inside the pre-chamber, which resulted in the initial asymmetry of the pre-chamber jets. At this point, the pre-chamber jets have attained the maximum flame surface area, i.e., the turbulent peripheral surface area of the jet is maximized just before they merge with one another causing the first peak in AHRR. The relative decrease in the observed intensities of the OH* chemiluminescence images (images: 1-9) throughout the combustion process with decreasing natural gas concentration in the main-chamber is to be expected as increasingly leaner mixtures lead to lower heat-release and OH* concentrations, along with reduced adiabatic flame temperatures. Furthermore, decreasing natural gas concentration in the main-chamber also reduces the total amount of fuel available to burn, resulting in lower AHRR values as expected.
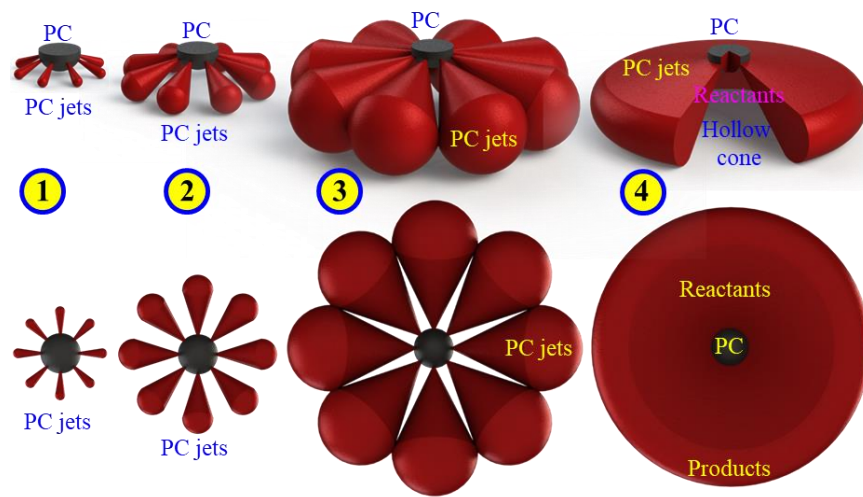
Figure 9. Schematic illustrating the sequence of development of pre-chamber jets and the subsequent consumption of main-chamber charge.

Beyond the first peak in AHRR, the pre-chamber jets begin to merge (image labels: 4-6) with one another, resulting in possible local extinction most likely caused by the unavailability of fresh reactants, leading to a sustained period (~3 CAD) of decreasing or plateauing AHRR lasting approximately until 355 CAD. Figure 9 illustrates schematically the combustion process in the main-chamber as the pre-chamber jets emerge, continue to penetrate, and ultimately merge with

one another in the main-chamber. As indicated in Figure 9, conceptually, at this point in the combustion process, the recently merged pre-chamber jets now structurally resemble a hollow cone with an open base. This hollow cone, primarily composed of hot products, separates two regions of fresh unreacted fuel-air mixture, one trapped between the hollow cone and the moving piston, while the other is enclosed between the hollow cone and the cylinder walls / head. These regions of trapped unreacted fresh fuel-air mixture appear primed for end gas auto-ignition as they are subjected to increasing pressure and temperature from compression, due to the heat release from the pre-chamber jets that has now consumed portions of the main-chamber charge, and due to the continued upward motion of the piston towards TDC (though minimal). The auto-ignition of the end gas results in rapid consumption of the air-fuel mixture resulting in the second peak in AHRR that is characterized by much higher chemiluminescence intensities (image labels: 7-9). The magnitude of the second peak in AHRR decreases with decreasing natural gas concentration in the main-chamber with extremely lean mixtures ($\lambda_{MC} > 2.2$ and above) resulting in a hardly discernible second peak. However, it is to be noted that the pressure profiles presented earlier do not present any evidence of high-frequency pressure oscillations that are typically associated with knocking combustion. This is most likely due to the pressure rise rates not being excessively high as the main-chamber charge composition is fairly lean throughout, leading to lower pressure and temperature when compared to stoichiometric combustion of natural gas [28]. The AHRR drops back to near zero levels around 370 CAD for most cases signifying the end of combustion process. However, for extremely lean mixtures ($\lambda_{MC} > 2.0$ and above), due to the decreased chemical reactivity of the mixture, the combustion process tends to proceed slowly and hence ends at around 375 CAD.

3.2.3. Mixing-controlled combustion vs kinetically-controlled combustion

Figure 10.(a) and 10.(b) show the individual AHRR traces (shown in a lighter color shade) for the 54 fired cycles of the fueled pre-chamber tests along with the ensemble averaged AHRR profiles (shown in a corresponding darker color shade). Figure 10.(c) shows the same data but with the AHRR scaled by the corresponding main-chamber air-fuel ratio (λ_{MC}) while using $\lambda_{MC} = 1.7$ as the baseline (nominal value). Following the same color scheme, Figure 11.(a) shows the cumulative heat release, while Figure 11.(b) presents the scaled version of the cumulative heat release, in which the cumulative heat release is scaled by the corresponding main-chamber air-fuel ratio (λ_{MC}) while using $\lambda_{MC} = 1.7$ as the baseline (nominal value). Figure 11.(c) shows the normalized cumulative heat release, where the values are normalized based on the corresponding maximum cumulative heat release.
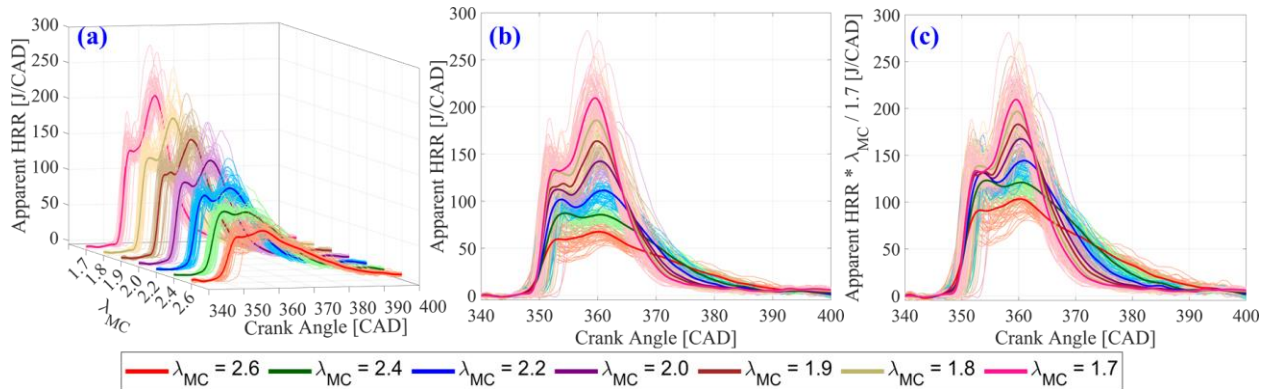
Figure 10. (a, b) Apparent heat release rate. (c) Apparent heat release rate scaled by λ_{MC} with $\lambda_{MC} = 1.7$ as the baseline condition for fueled pre-chamber experiments. λ_{PC} is held constant at 0.93 for varying λ_{MC}. The individual 54 fired cycles are shown in a lighter color shade with the corresponding darker color shade indicating the ensemble averaged results.
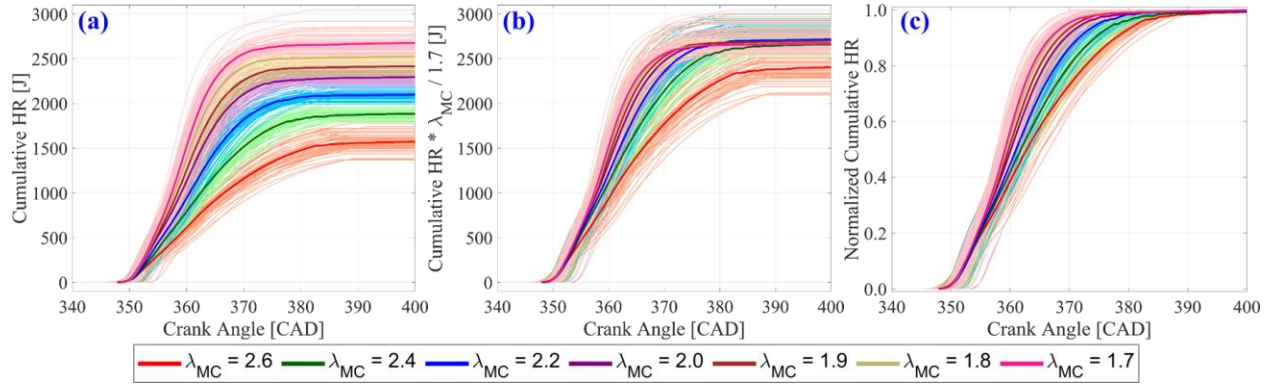
Figure 11. (a) Cumulative heat release. (b) Cumulative heat release scaled by λ_{MC} with λ_{MC} = 1.7 as the baseline condition. (c) Normalized cumulative heat release for fueled pre-chamber experiments. λ_{PC} is held constant at 0.93 for varying λ_{MC}. The individual 54 fired cycles are shown in a lighter color shade with the corresponding darker color shade indicating the ensemble averaged results.

From Figure 10 and Figure 11, it is clear that the timing of the start of combustion remains fairly consistent within the levels of cycle-to-cycle variation observed at each dataset, despite the wide range of natural gas concentrations (as λ_{MC} is varied from 1.7 to 2.6) inside the main-chamber. However, the timing of the end of combustion exhibits a slight dependence on natural gas concentration inside the main-chamber, which results in a slight longer combustion duration (not exceeding 10 CAD) for ultra-lean mixtures.

Figure 10.(c) shows that the first peak of the scaled AHRR (first-stage heat release) collapses to around 130 J/CAD for most cases while it reaches slightly lower values of 120 J/CAD and 90 J/CAD for λ_{MC} = 2.4 and 2.6, respectively. This is in part due to the near identical nature of the pre-chamber jet development and mixing characteristics that are solely determined by the air-fuel ratio in the pre-chamber, which is held constant throughout. The pre-chamber jets' exit velocity is estimated to be in the range of 150 - 200 m/s, while the tip penetration speed is calculated to be lower around 100 m/s mainly due to entrainment and viscosity effects [30, 31, 51]. These values were computed based on the sequential high-speed OH* chemiluminescence images [30, 31, 51] just as the pre-chamber jets emerge into the main-chamber (first few frames) and

continue to penetrate further downstream (subsequent frames), respectively, and are found to be nearly independent of the main-chamber natural gas concentration. These estimated values are at least one to two orders of magnitude higher than the highest achievable turbulent flame speed under these engine conditions [52, 53]. Thus, it is conceivable that the combustion process during the first-stage of heat release is jet-momentum driven and mixing controlled (until the first peak in AHRR). Thus, the majority of main-chamber charge is consumed predominantly due to the penetration of pre-chamber jets (controlled by the pressure-difference) and the subsequent entrainment of the main-chamber charge, rather than due to flame propagation or sequential auto-ignition (kinetically-controlled combustion). This type of pre-chamber mixing-controlled combustion is distinctly different from diesel combustion, i.e., it is not the mixing of fuel with air, but rather the mixing of hot-burned gases with unburned fuel-air mixture that seems to be controlling the rate of combustion, and is largely independent of flame speed. Also, since the air-fuel ratio in the pre-chamber is held constant throughout, the pre-chamber jet penetration and the mass of natural gas air-charge entrained from the main-chamber remains identical, causing the first peak of AHRR to collapse when scaled appropriately by λ_{MC}. The deviations observed in the ultra-lean cases might possibly be due to decreased reactivity or incomplete combustion of the entrained main-chamber charge.

However, Figure 10.(c) shows that the second peak of the scaled AHRR (second-stage heat release) does not collapse when rescaled by λ_{MC}. It is to be noted that by this point in the AHRR, there is negligible pressure difference ($\Delta P \sim 0$) between the pre-chamber and the main-chamber, i.e., no driving force behind the pre-chamber jets. This most likely suggests the end of jet-momentum driven, mixing-controlled combustion phase (first-stage heat release) and the onset or transition into more of a kinetically-controlled combustion phase or potential turbulent flame

propagation (second-stage heat release). Figure 12 compares the similarities and differences in the normalized cumulative heat release at key crank-angle timings (based on ΔP and AHRR) and combustion phasing during the transition between the mixing-controlled and kinetically-controlled combustion phases. From Figure 12.(a), it is clear that there is no discernible difference in the normalized cumulative heat release across all λ_{MC} during the entirety of the mixing-controlled combustion phase that involves the development of pre-chamber ($\Delta P > 0.5$ bar, max ΔP, $\Delta P \sim 0$ bar) and the subsequent first peak in AHRR. This is also in line with start of combustion and the subsequent combustion phasing (CA10 through CA50) being almost independent of the natural gas concentration in the main-chamber as shown in Figure 12.(b). However, beyond this point, i.e., the onset of kinetically-controlled combustion, these observed trends begin to diverge as they start to exhibit a minor dependence on natural gas concentration in the main-chamber. This is clearly shown by the variation in cumulative heat release rate at 360 CAD (second peak in AHRR) and the combustion phasing beyond CA50 with λ_{MC} as presented in Figure 12.(a) and (b), respectively.
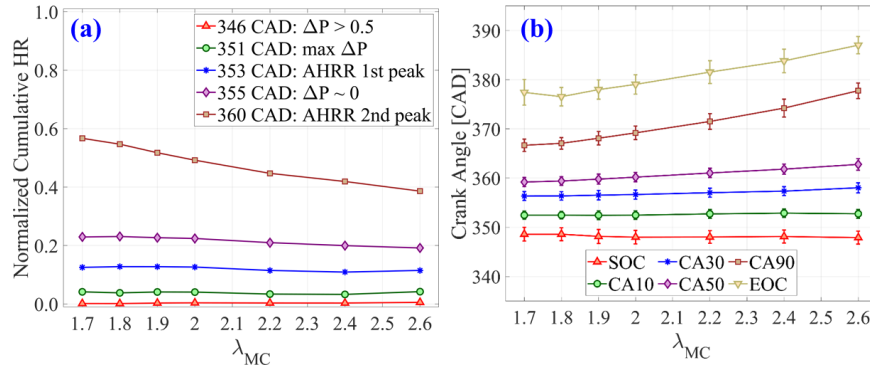

Figure 12. (a) Normalized cumulative heat release at key crank angle timings (as indicated by the legend) during the combustion process. (b) Timing of key combustion events (combustion phasing) for fueled pre-chamber experiments. λ_{PC} is held constant at 0.93 for varying λ_{MC}.

3.2.4. CHEMKIN Simulations

As hypothesized in the previous sections, the second peak observed in the AHRR is possibly due to auto-ignition of the end gas mixture. However, this second peak in AHRR and the

subsequent combustion process exhibits several interesting features. It is clear from Figure 10.(c) that, unlike the first peak, the second peak in AHRR does not collapse when scaled by λ_{MC} appropriately, and by this point in the combustion process, there is negligible pressure difference between the pre-chamber and the main-chamber as shown in Figure 8. This most likely suggests the end of jet-momentum driven, mixing-controlled combustion and the transition into more of a kinetically-controlled combustion phase. To confirm this hypothesis, a zero-dimensional (0-D) homogenous reactor model-based chemical kinetics simulation was carried out with Ansys CHEMKIN-Pro package using the AramcoMech 2.0 version [54] to predict the combustion duration after the proposed onset of this kinetically-controlled combustion phase, i.e., second peak of AHRR. This potentially "kinetically-controlled combustion phase" was modeled in a closed adiabatic reactor, i.e., no mass or heat exchange with the surroundings, using three distinct simulation approaches as highlighted in Figure 13, namely (i) constant pressure, (ii) constant volume, and (iii) constrained pressure profile simulations by imposing the dynamic main-chamber pressure trajectory from the experiments.
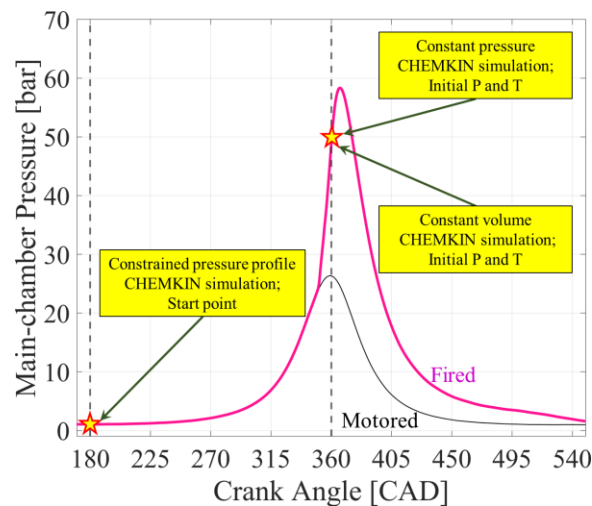

Figure 13. Schematic elucidating the three different approaches (constant pressure, constant volume, constrained pressure) adopted for the 0-D CHEMKIN simulations indicating the reactor initial conditions.

For constant pressure and constant volume simulations, the reactor was initialized with varying concentrations of natural gas-air charge with the initial pressure and temperature based on the corresponding values of ensemble averaged main-chamber pressure at the time of the second peak in AHRR (~ 360 CAD) and the estimated isentropic compression temperature, respectively. For constrained pressure profile simulations, the reactor was initialized with varying concentrations of natural gas-air charge with initial pressure and temperature based on the corresponding values of ensemble-averaged main-chamber pressure measured at BDC and the estimated temperature at BDC, respectively. The BDC temperature (T_{BDC}) was estimated to be 331 K based on the intake charge temperature (T_{in} = 41ºC) and coolant temperature (T_{cool} = 95ºC) as per T_{BDC} = 0.68*(T_{in} - T_{cool}) + T_{cool} [43]. The reactor pressure was then constrained by imposing the ensemble averaged, measured, dynamic main-chamber pressure trajectory from the experiments. Thus, this approach simulated a portion of the main-chamber charge as-yet unburned fuel-air charge (end-gas) that experiences no heat transfer and is compressed by the movement of the piston and/or the expansion of hot gases created by the combustion due to the pre-chamber jets. This approach is most representative of portions of the charge that are outside the boundary layers near the walls, and thus experience low heat transfer losses. This formulation also does not account for heat or mass transfer from the pre-chamber jets, and essentially represents regions that are not in close proximity to the edge of the pre-chamber jets, i.e., hollow cone as described in Figure 9.

The evolution of temperature for the three different CHEMKIN simulation approaches described earlier are shown in Figure 14.(a), (b) and (c), respectively, for various λ_{MC} with markers indicating the timing of CA10, CA50, and CA90 calculated based on the cumulative heat release. From Figure 14.(a) and (b), it can be clearly seen that the constant pressure and constant volume

simulation approaches yield unrealistically long ignition delays exceeding 180ºCA for even the most reactive mixture (λ_{MC} = 1.7). Given the unrealistic ignition delay estimates of the constant pressure and constant volume approaches, further simulations employed the constrained pressure profile approach exclusively. However, the reactor temperatures did not exceed motoring levels (~900 K) irrespective of the natural gas concentration for the constrained pressure profile simulations as seen in Figure 14.(c), indicating that the fuel-air mixture does not auto-ignite under these conditions.
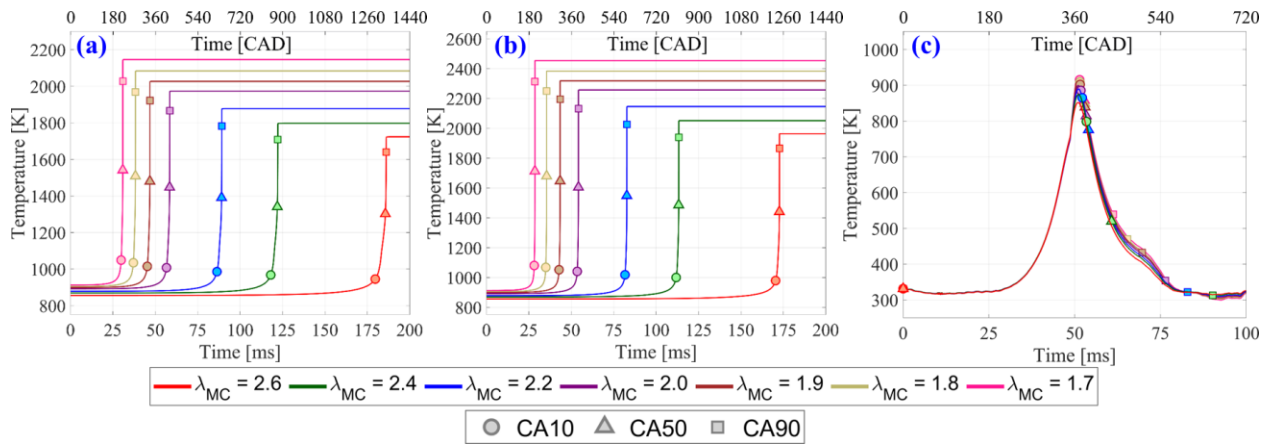
Figure 14. Temperature profile based on CHEMKIN simulations under (a) constant pressure, (b) constant volume, and (c) constrained experimental pressure profile for varying λ_{MC}. Markers on each temperature profile indicate CA10, CA50 and CA90.

The intake temperature of the fuel-air mixture was then increased artificially in increments of 5ºC to explore the possibility of auto-ignition under the constrained pressure profile approach. To achieve auto-ignition across all λ_{MC}, it was estimated that the intake temperature of the fuel-air mixture had to be artificially increased to a minimum of 235ºC (T_{BDC} = 463 K). The corresponding temperature, cumulative heat release, and cumulative heat release scaled by λ_{MC} with λ_{MC} = 1.7 as the baseline are shown in Figure 15.(a), (b), and (c), respectively. The markers on these profiles again indicate the positions of CA10, CA50, and CA90. From Figure 15, it can be clearly seen that the fuel-air mixture does auto-ignite with realistic ignition delay that increases with λ_{MC} values
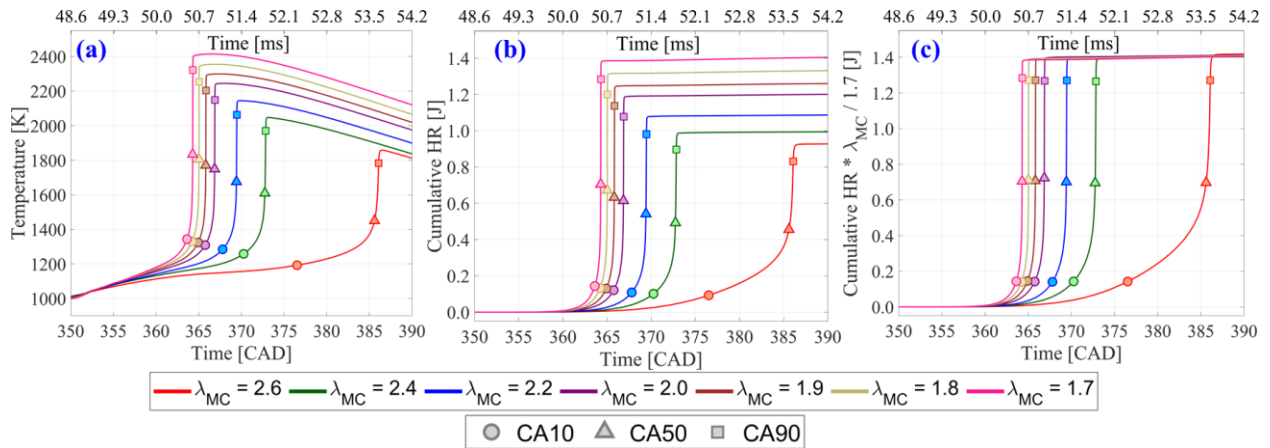
under these conditions.

Figure 15. (a) Temperature profile (b) Cumulative heat release rate (c) Cumulative heat release rate scaled by λ_{MC} with λ_{MC} = 1.7 as the baseline condition based on CHEMKIN simulations with constrained (imposed) experimental pressure profile.

Figure 16 compares the CA50 timing of the left-over charge between fueled pre-chamber experiments (T_{in} = 41ºC, T_{BDC} = 331 K) and constrained profile CHEMKIN simulations with artificially increased fuel-air mixture intake temperature (T_{in} = 235ºC, T_{BDC} = 463 K) for varying λ_{MC}. With an artificially increased fuel-air mixture intake temperature of 235ºC, the constrained profile CHEMKIN simulations based CA50 timing was found to vary between 364 CAD (λ_{MC} = 1.7) and 386 CAD (λ_{MC} = 2.6) based on the natural gas concentration. This, however, is in stark contrast to experiments, which were conducted at considerably lower fuel-air mixture intake temperature of 41ºC, as they exhibited comparable CA50 timing (for the left-over charge after the first peak in AHRR) of 363 CAD (within 3 CAD) despite the wide range of natural gas concentration in the main-chamber. Thus, the combination of comparable experimental CA50 timings, almost independent of λ_{MC}, along with the necessity to artificially increase intake fuel-air mixture temperatures to unrealistically high values to achieve auto-ignition in CHEMKIN simulations, do not support the onset of kinetically-controlled combustion in the second phase of heat-release in fueled pre-chamber experiments. This suggests that there exists some degree of

sustained mixing-controlled combustion throughout the entire combustion process, though the reason for this is not clear at this point and is most likely attributed to the in-cylinder bulk flow and the associated turbulence. However, the increasing combustion duration for leaner mixtures is most likely due to a steady transition along the spectrum towards a more kinetically-controlled combustion for leaner mixtures. Thus, when the mixtures are too lean, even if mixing remains fast enough to bring hot gases to ignite all of the unburned fuel, chemical kinetics may be too slow to complete combustion before expansion cooling.
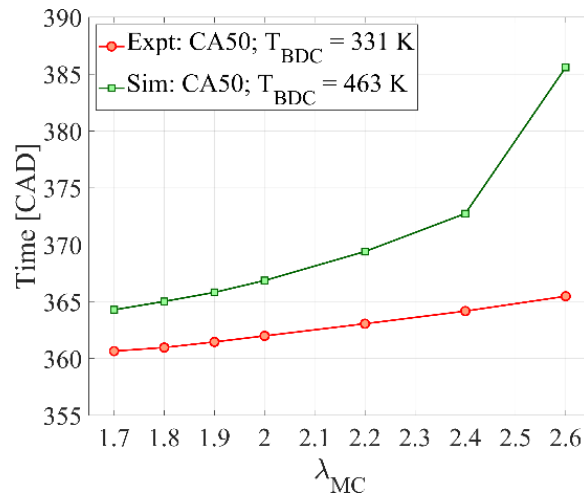

Figure 16. Comparison of CA50 timing of the left-over charge between fueled pre-chamber experiments (T_{in} =41ºC, T_{BDC} = 331 K) and constrained profile CHEMKIN simulations (artificially increased T_{in} =235ºC, T_{BDC} = 463 K) for varying λ_{MC}.

4. Conclusions

Experiments were performed in a heavy-duty, optical, single-cylinder engine fitted with an actively fueled pre-chamber spark-ignition module to provide fundamental insights on the underlying fluid-mechanical and chemical-kinetic processes that govern the ignition and subsequent combustion of natural gas near lean-limits in high-efficiency lean-burn natural gas engines employing PCSI system. The spatial and temporal progress of ignition and combustion of lean-burn of natural gas using PCSI system were studied using optical diagnostic imaging and heat

release analysis based on main-chamber and pre-chamber pressure measurements. Optical diagnostics involving simultaneous infrared and chemiluminescence imaging helped in identifying key phenomenological features of the pre-chamber ignition systems. This revealed how the pre-chamber ignition-jet emerges from the pre-chamber, mixes with and ignites the premixed main-chamber gases, and subsequently drives the progression of main-chamber combustion, whether by flame propagation or sequential auto-ignition.

Analysis of experimental results support the following conclusions:

1. There is a clear lag in pressure-equilibration between the pre-chamber and main-chamber pressures even in the absence of combustion despite continuous gas-exchange.

2. In pre-chamber only fueling experiments with no natural gas in the main-chamber, the observed cycle-to-cycle variability both in terms of magnitude (ΔP_{max}: 13.49 - 22.13 bar; COV ~ 10.72%) and corresponding CAD timing (ΔP_{max} @ 348.75 - 351.75 CAD) is most likely due to a combination of intense turbulence-induced stratification of the pre-chamber charge caused by the fuel injection event and the non-uniformities in the flame kernel development inside the pre-chamber.

3. Composite snapshots of IR and broadband chemiluminescence from pre-chamber only fueling experiments reveal two distinct regions that constitute a transient pre-chamber jet after initial ejection of the unreacted fuel-air mixture caused by pre-chamber pressure rise: a localized reactive region restricted to the pre-chamber periphery, and a far-reaching, widespread non-reactive region composed primarily of hot products. Charge stratification and stochastic nature of ignition lead to spatial and temporal asymmetry in the development of pre-chamber jets.

4. In fueled pre-chamber experiments, despite varying λ_{MC}, the primary driving force (ΔP) that governs the formation, development, and subsequent mixing of the pre-chamber jets with the

contents of the main-cylinder is essentially identical (ΔP_{max} = 13.13 bar at 350.75 CAD for λ_{MC} = 1.7 with COV = 14.65%; ΔP_{max} = 12.70 bar at 351 CAD for λ_{MC} = 2.6 with COV = 17.92%) as it is almost entirely dictated by λ_{PC}, which is maintained constant throughout.

5. The consistent emergence of pre-chamber jets at similar crank angle timing (349.5 CAD, ΔP ~ 3 bar), despite varying λ_{MC}, as revealed by the composite snapshots, also supports the hypothesis stated above.

6. The AHRR profiles clearly exhibit similarities in terms of start, end, and duration of combustion, in addition to its two-stage heat release feature irrespective of λ_{MC}. The local minimum in the AHRR is coincident with the pre-chamber jets merging (resembling a hollow cone with an open base) causing possible local extinction due to unavailability of fresh reactants. The second peak in AHRR is hypothesized to be most likely due to auto-ignition of end gas causing rapid consumption of the remaining mixture.

7. The scaling of the first peak of AHRR with λ_{MC}, and the estimated pre-chamber jets' exit velocity (~ 150 - 200 m/s) and tip penetration speed (~ 100 m/s) exceeding highest achievable turbulent flame speeds under such conditions by one to two orders of magnitude, suggest an initial jet-momentum driven, mixing-controlled premixed combustion phase.

8. The incompatible scaling of the second peak of AHRR with λ_{MC} and the non-existent driving force (ΔP ~ 0) behind the pre-chamber jets suggested a possible transition from a mixing-controlled to a kinetically-controlled combustion phase.

9. Detailed chemical kinetics simulations indicated either unrealistically long ignition delays for constant pressure and constant volume approaches or failure to auto-ignite under constrained pressure approach using the actual intake temperature. Even when intake temperature was artificially increased to achieve auto-ignition, the resulting combustion process showed a

strong dependence on λ_{MC}, which is in stark contrast to the experimentally observed near identical combustion durations that suggests a sustained mixing-controlled combustion to at least some degree throughout the entire combustion process.

Based on these experimental observations, some key elements for an initial conceptual model for ignition of fuel-lean main-chamber mixtures by a near-stoichiometric pre-chamber are outlined as follows:

1. Unburned fuel mixture is pushed out of the pre-chamber before main-chamber ignition, creating a spatially symmetric unburned turbulent fuel-jet pattern in the main chamber.

   a. Variations in IR intensity among the jets suggest non-uniform fuel mixtures in the bottom of the pre-chamber.

   b. Incomplete mixing of pre-chamber injected fuel, as well as incomplete mixing with main-chamber gas pushed into the pre-chamber during the compression stroke, may both contribute to non-uniform initial pre-chamber unburned jet mixtures.

2. Main-chamber ignition is generally asymmetric as combustion emerges from the pre-chamber at different times in different jets.

   a. This is consistent with non-uniform flame propagation inside the neck of the pre-chamber, even though the proximity of orifices to each other is much less than their distance from the spark plug.

3. The combustion heat release generally occurs in two stages with an observable dip in AHRR between them.

   a. The first stage heat release is smaller and shorter in duration, and its AHRR peak seems to occur when the adjacent burning pre-chamber jets merge as they consume the fresh-charge between them.

i. Combustion up to the first AHRR peak seems to be mixing controlled, driven by jet turbulence/momentum.

- The initial collapse of cumulative heat-release across λ_{MC} suggests that initial main-chamber heat release is mixing controlled.

- This collapse is inconsistent with flame propagation (would be slower at leaner λ_{MC}).

- This type of pre-chamber mixing-controlled combustion is different from that of diesel combustion, as it is not the mixing of fuel with air, but rather the mixing of hot-burned gases with unburned fuel-air mixture that seems to be controlling the rate of combustion, largely independent of flame speed.

b. The second stage heat release is more intense and longer in duration.

i. This second stage heat release also seems to be mixing controlled, potentially driven by the in-cylinder bulk flow and the associated turbulence. However, it is also increasingly moderated by chemical kinetics as main-chamber mixtures become leaner.

- The rate of combustion seems too fast for either flame propagation or auto-ignition though their relative contribution in the later stages of combustion may indeed be significant.

- The relatively small variation in the rate of combustion with λ_{MC} is also inconsistent with expected trends for flame propagation or auto-ignition (kinetics controlled).

- Increasing combustion duration with increasingly fuel-lean main-chamber mixtures may be due to a transition along the spectrum to more kinetically-controlled combustion for leaner mixtures.

4. As the main-chamber lean-limit is approached, the general picture of combustion processes

seems to remain essentially unchanged, yet an increasing fraction of the fuel does not burn as the combustion duration becomes very long, extending well into the expansion stroke.

a. Even if mixing remains fast enough to bring hot gases to ignite all of the unburned fuel, when the mixtures are very lean, chemical kinetics may be too slow to complete combustion before expansion cooling.

5. Acknowledgments

6. References

[1] International Energy Outlook: DOE/EIA-0484 (2016), US Department of Energy, May 2016, May 2016.
[2] March 2020 Monthly Energy Review. Technical Report DOE/EIA-0035(2020/3), US Department of Energy, March 2020.
[3] R.P. Roethlisberger, D. Favrat, Comparison between direct and indirect (prechamber) spark ignition in the case of a cogeneration natural gas engine, part I: engine geometrical parameters, Applied Thermal Engineering 22 (2002) 1217-1229.
[4] R.P. Roethlisberger, D. Favrat, Comparison between direct and indirect (prechamber) spark ignition in the case of a cogeneration natural gas engine,: part II: engine operating parameters and turbocharger characteristics, Applied Thermal Engineering 22 (2002) 1231-1243.

[5] R.P. Roethlisberger, D. Favrat, Investigation of the prechamber geometrical configuration of a natural gas spark ignition engine for cogeneration: part I. Numerical simulation, International Journal of Thermal Sciences 42 (2003) 223-237.

[6] R.P. Roethlisberger, D. Favrat, Investigation of the prechamber geometrical configuration of a natural gas spark ignition engine for cogeneration: part II. Experimentation, International Journal of Thermal Sciences 42 (2003) 239-253.

[7] A. Shah, P. Tunestal, B. Johansson, Effect of Pre-Chamber Volume and Nozzle Diameter on Pre-Chamber Ignition in Heavy Duty Natural Gas Engines, SAE Technical Paper, 2015-01-0867, doi:10.4271/2015-01-0867(2015).

[8] A. Shah, P. Tunestal, B. Johansson, Effect of Relative Mixture Strength on Performance of Divided Chamber 'Avalanche Activated Combustion' Ignition Technique in a Heavy Duty Natural Gas Engine, SAE Technical Paper, 2014-01-1327, doi:10.4271/2014-01-1327(2014).

[9] X. Li, W. Zhang, Z. Huang, D. Ju, L. Huang, M. Feng, X. Lu, Z. Huang, Pre-chamber turbulent jet ignition of methane/air mixtures with multiple orifices in a large bore constant volume chamber: effect of air-fuel equivalence ratio and pre-mixed pressure, Frontiers in Energy 13 (2019) 483-493.

[10] E.-S. Cho, S.H. Chung, Improvement of flame stability and NOx reduction in hydrogen-added ultra lean premixed combustion, Journal of Mechanical Science and Technology 23 (2009) 650-658.

[11] L.A. Graham, S.L. Belisle, P. Rieger, Nitrous oxide emissions from light duty vehicles, Atmospheric Environment 43 (2009) 2031-2044.

[12] W.P. Attard, H. Blaxill, A Lean Burn Gasoline Fueled Pre-Chamber Jet Ignition Combustion System Achieving High Efficiency and Low NOx at Part Load, SAE Technical Paper, 2012-01-1146, doi:10.4271/2012-01-1146(2012).

[13] W.P. Attard, H. Blaxill, A Gasoline Fueled Pre-Chamber Jet Ignition Combustion System at Unthrottled Conditions, SAE International Journal of Engines 5 (2012) 315-329.

[14] W.P. Attard, M. Bassett, P. Parsons, H. Blaxill, A New Combustion System Achieving High Drive Cycle Fuel Economy Improvements in a Modern Vehicle Powertrain, SAE Technical Paper, 2011-01-0664, doi:10.4271/2011-01-0664(2011).

[15] J. Benajes, R. Novella, J. Gomez-Soriano, P.J. Martinez-Hernandiz, C. Libert, M. Dabiri, Evaluation of the passive pre-chamber ignition concept for future high compression ratio turbocharged spark-ignition engines, Applied Energy 248 (2019) 576-588.

[16] G.J. Germane, C.G. Wood, C.C. Hess, Lean Combustion in Spark-Ignited Internal Combustion Engines - A Review, SAE Technical Paper, 831694, doi:10.4271/831694(1983).

[17] A.A. Quader, Lean Combustion and the Misfire Limit in Spark Ignition Engines, SAE Technical Paper, 741055, doi:10.4271/741055(1974).

[18] H. Reddy, J. Abraham, Ignition kernel development studies relevant to lean-burn natural-gas engines, Fuel 89 (2010) 3262-3271.

[19] A. Das, H.C. Watson, Development of a natural gas spark ignition engine for optimum performance, Proceedings of the Institution of Mechanical Engineers, Part D: Journal of Automobile Engineering 211 (1997) 361-378.

[20] G.A. Karim, A review of combustion processes in the dual fuel engine—The gas diesel engine, Progress in Energy and Combustion Science 6 (1980) 277-285.

[21] G.A. Karim, Combustion in Gas Fueled Compression: Ignition Engines of the Dual Fuel Type, Journal of Engineering for Gas Turbines and Power 125 (2003) 827-836.

[22] R. Rajasegar, Y. Niki, Z. Li, J.M. García-Oliver, M.P.B. Musculus, Influence of pilot-fuel mixing on the spatio-temporal progression of two-stage autoignition of diesel-sprays in low-

reactivity ambient fuel-air mixture, Proceedings of the Combustion Institute 38 (2021) 5741-5750.

[23] Y. Niki, R. Rajasegar, Z. Li, M.P. Musculus, J.M. Garcia Oliver, K. Takasaki, Verification of diesel spray ignition phenomenon in dual-fuel diesel-piloted premixed natural gas engine, International Journal of Engine Research, doi:10.1177/1468087420983060 1468087420983060.

[24] R. Rajasegar, Y. Niki, J.M. Garcia-Oliver, Z. Li, M. Musculus, Spatio-Temporal Progression of Two-Stage Autoignition for Diesel Sprays in a Low-Reactivity Ambient: n-Heptane Pilot-Ignited Premixed Natural Gas, SAE Technical Paper, 2021-01-0525, doi:10.4271/2021-01-0525(2021).

[25] C.E.C. Alvarez, G.E. Couto, V.R. Roso, A.B. Thiriet, R.M. Valle, A review of prechamber ignition systems as lean combustion technology for SI engines, Applied Thermal Engineering 128 (2018) 107-120.

[26] E. Toulson, H.J. Schock, W.P. Attard, A Review of Pre-Chamber Initiated Jet Ignition Combustion Systems, SAE Technical Paper, 2010-01-2263, doi:10.4271/2010-01-2263(2010).

[27] E.K. Anderson, W.P. Attard, A. Brown, P. Litke, K. Grinstead, J. Hoke, Experimental Study of a Pre-Chamber Jet Igniter in a Turbocharged Rotax 914 Aircraft Engine, SAE Technical Paper, 2013-01-1629, doi:10.4271/2013-01-1629(2013).

[28] G. Gentz, M. Gholamisheeri, E. Toulson, A study of a turbulent jet ignition system fueled with iso-octane: Pressure trace analysis and combustion visualization, Applied Energy 189 (2017) 385-394.

[29] J.D. Dale, M.D. Checkel, P.R. Smy, Application of high energy ignition systems to engines, Progress in Energy and Combustion Science 23 (1997) 379-398.

[30] G. Gentz, B. Thelen, M. Gholamisheeri, P. Litke, A. Brown, J. Hoke, E. Toulson, A study of the influence of orifice diameter on a turbulent jet ignition system through combustion visualization and performance characterization in a rapid compression machine, Applied Thermal Engineering 81 (2015) 399-411.

[31] M. Gholamisheeri, I.S. Wichman, E. Toulson, A study of the turbulent jet flow field in a methane fueled turbulent jet ignition (TJI) system, Combustion and Flame 183 (2017) 194-206.

[32] S. Biswas, L. Qiao, Ignition of ultra-lean premixed H2/air using multiple hot turbulent jets generated by pre-chamber combustion, Applied Thermal Engineering 132 (2018) 102-114.

[33] S. Yamaguchi, N. Ohiwa, T. Hasegawa, Ignition and burning process in a divided chamber bomb, Combustion and Flame 59 (1985) 177-187.

[34] P.M. Allison, M. de Oliveira, A. Giusti, E. Mastorakos, Pre-chamber ignition mechanism: Experiments and simulations on turbulent jet flame structure, Fuel 230 (2018) 274-281.

[35] E. Toulson, A. Huisjen, X. Chen, C. Squibb, G. Zhu, H. Schock, W.P. Attard, Visualization of Propane and Natural Gas Spark Ignition and Turbulent Jet Ignition Combustion, SAE International Journal of Engines 5 (2012) 1821-1835.

[36] W.P. Attard, E. Toulson, A. Huisjen, X. Chen, G. Zhu, H. Schock, Spark Ignition and Pre-Chamber Turbulent Jet Ignition Combustion Visualization, SAE Technical Paper, 2012-01-0823, doi:10.4271/2012-01-0823(2012).

[37] A. Shah, P. Tunestal, B. Johansson, Investigation of Performance and Emission Characteristics of a Heavy Duty Natural Gas Engine Operated with Pre-Chamber Spark Plug and Dilution with Excess Air and EGR, SAE International Journal of Engines 5 (2012) 1790-1801.

[38] Natural Gas Vehicle Research Workshop, U.S. Department of Energy - Vehicle Technologies Office. https://www.nrel.gov/transportation/ngv-research-workshop.html, July 2017

[39] C.L. Genzale, R.D. Reitz, M.P.B. Musculus, Optical Diagnostics and Multi-Dimensional Modeling of Spray Targeting Effects in Late-Injection Low-Temperature Diesel Combustion, SAE

Technical Paper, 2009-01-2699, doi:10.4271/2009-01-2699(2009).

[40] J.E. Dec, A Conceptual Model of DI Diesel Combustion Based on Laser-Sheet Imaging*, SAE Technical Paper, 970873, doi:10.4271/970873(1997).

[41] C. Espey, J.E. Dec, Diesel Engine Combustion Studies in a Newly Designed Optical-Access Engine Using High-Speed Visualization and 2-D Laser Imaging, SAE Technical Paper, 930971, doi:10.4271/930971(1993).

[42] J.B. Heywood, Internal combustion engine fundamentals, New York : McGraw-Hill, [1988] ©19881988.

[43] S.L. Kokjohn, M.P.B. Musculus, R.D. Reitz, Evaluating temperature and fuel stratification for heat-release rate control in a reactivity-controlled compression-ignition engine using optical diagnostics and chemical kinetics modeling, Combustion and Flame 162 (2015) 2729-2742.

[44] L.M. Pickett, D.L. Siebers, C.A. Idicheria, Relationship Between Ignition Processes and the Lift-Off Length of Diesel Fuel Jets, SAE Technical Paper, 2005-01-3843, doi:10.4271/2005-01-3843(2005).

[45] D.L. Siebers, B. Higgins, Flame Lift-Off on Direct-Injection Diesel Sprays Under Quiescent Conditions, SAE Technical Paper, 2001-01-0530, doi:10.4271/2001-01-0530(2001).

[46] H. Anders, M. Christensen, B. Johansson, A. Franke, M. Richter, M. Aldén, A Study of the Homogeneous Charge Compression Ignition Combustion Process by Chemiluminescence Imaging, SAE Technical Paper, 1999-01-3680, doi:10.4271/1999-01-3680(1999).

[47] J.E. Dec, W. Hwang, M. Sjöberg, An Investigation of Thermal Stratification in HCCI Engines Using Chemiluminescence Imaging, SAE Technical Paper, 2006-01-1518, doi:10.4271/2006-01-1518(2006).

[48] M. Gholamisheeri, B. Thelen, G. Gentz, E. Toulson, CFD Modeling of an Auxiliary Fueled Turbulent Jet Ignition System in a Rapid Compression Machine, SAE Technical Paper, 2016-01-0599, doi:10.4271/2016-01-0599(2016).

[49] B.C. Thelen, G. Gentz, E. Toulson, Computational Study of a Turbulent Jet Ignition System for Lean Burn Operation in a Rapid Compression Machine, SAE Technical Paper, 2015-01-0396, doi:10.4271/2015-01-0396(2015).

[50] M.P.B. Musculus, K. Kattke, Entrainment Waves in Diesel Jets, SAE International Journal of Engines 2 (2009) 1170-1193.

[51] M. Gholamisheeri, B.C. Thelen, G.R. Gentz, I.S. Wichman, E. Toulson, Rapid compression machine study of a premixed, variable inlet density and flow rate, confined turbulent jet, Combustion and Flame 169 (2016) 321-332.

[52] P. Griebel, P. Siewert, P. Jansohn, Flame characteristics of turbulent lean premixed methane/air flames at high pressure: Turbulent flame speed and flame brush thickness, Proceedings of the Combustion Institute 31 (2007) 3083-3090.

[53] A. Ratzke, T. Schöffler, K. Kuppa, F. Dinkelacker, Validation of turbulent flame speed models for methane–air-mixtures at high pressure gas engine conditions, Combustion and Flame 162 (2015) 2778-2787.

[54] W.K. Metcalfe, S.M. Burke, S.S. Ahmed, H.J. Curran, A Hierarchical and Comparative Kinetic Modeling Study of C1− C2Hydrocarbon and Oxygenated Fuels, International Journal of Chemical Kinetics 45 (2013) 638-675.